



## 5G Communication with a Heterogeneous, Agile Mobile network in the Pyeongchang Winter Olympic competition

Grant agreement n. 723247

# Deliverable D3.8 Final results on the mobility framework

<b>Date of Delivery:</b>	31 May 2018 (Contractual)	25 May 2018 (Actual)
<b>Editor:</b>	Gosan Noh (ETRI)	
<b>Associate Editors:</b>		
<b>Authors:</b>	Gosan Noh (ETRI), Junhyeong Kim (ETRI), Bing Hui (ETRI), Ilgyu Kim (ETRI), Mathis Schmieder (HHI), Antonio De Domenico (CEA)	
<b>Dissemination Level:</b>	PU	
<b>Security:</b>	Public	
<b>Status:</b>	Final	
<b>Version:</b>	V1.0	
<b>File Name:</b>	D3.8	
<b>Work Package:</b>	WP3	



---

**Title:** Deliverable D3.8: Final results on the mobility framework  
**Date:** 31 May 2018      **Status:** Final  
**Security:** Public      **Version:** V1.0

---

Modifications	Date	Version
Initial document	7 May 2018	0.1
Final document	25 May 2018	1.0

### Abstract

This deliverable provides refined channel model suitable for mobile backhaul. The channel model is based both on ray tracing of a realistic train deployment scenario and actual measurement campaign. This deliverable also includes the finalized architecture for the moving hotspots and the related mobility management algorithms, including the positioning and data-rate trade-off analysis, coverage analysis, random access, and handover triggering of high speed train scenario.

### Index terms

5G, mmWave channel modelling, high mobility management, mobility algorithms



---

<b>Title:</b>	Deliverable D3.8: Final results on the mobility framework		
<b>Date:</b>	31 May 2018	<b>Status:</b>	Final
<b>Security:</b>	Public	<b>Version:</b>	V1.0

---

## Contents

<b>1</b>	<b>Introduction .....</b>	<b>8</b>
<b>2</b>	<b>mmWave channel modeling for high mobility .....</b>	<b>9</b>
2.1	<i>Channel measurement and modeling of a rural 28 GHz HST scenario (HHI)</i>	9
2.2	<i>MHN-E channel measurement and modeling (ETRI)</i>	18
2.3	<i>Link-level performance evaluation of MHN-E system for high-speed train communications (ETRI)</i>	21
<b>3</b>	<b>Analyzing the Positioning Data-Rate Trade-off in mm-Wave communications through Stochastic Geometry (CEA) .....</b>	<b>31</b>
3.1	<i>Introduction</i>	31
3.2	<i>System Model</i>	32
3.3	<i>Positioning Error, Data Rate Coverage, and Misalignment Error</i>	33
3.4	<i>Numerical Results and Discussion</i>	35
<b>4</b>	<b>Mobility management techniques and architecture .....</b>	<b>39</b>
4.1	<i>Coverage analysis and performance evaluation of HST under linear deployment architecture (ETRI)</i>	39
4.2	<i>Random access performance evaluation and handover triggering for HST (ETRI)</i>	44
<b>5</b>	<b>Conclusion.....</b>	<b>53</b>
<b>6</b>	<b>References.....</b>	<b>54</b>



---

<b>Title:</b>	Deliverable D3.8: Final results on the mobility framework		
<b>Date:</b>	31 May 2018	<b>Status:</b>	Final
<b>Security:</b>	Public	<b>Version:</b>	V1.0

---

## List of Acronyms

3GPP	3rd Generation Partnership Project
5G	5th Generation
AFC	Automatic Frequency Control
AoA	Angle of Arrival
APDP	Averaged Power Delay Profile
ASA	Azimuth Angle Spread of Arrival
AWGN	Additive White Gaussian Noise
BBU	Baseband Unit
BCRLB	Bayesian Cramer-Rao Lower Bound
BS	Base Station
CA	Carrier Aggregation
CC	Component Carrier
CDF	Cumulative Distribution Function
CIR	Channel Impulse Responce
CP	Cyclic Prefix
CSI	Channel State Information
CSI-RS	CSI Reference Signal
DS	Delay Spread
DL	Downlink
FSPL	Free-Space Path Loss
FZC	Franz-Zadoff-Chu Sequence
GSCM	Geometry-based Stochastic Channel Model
GT	Guard Time
gNB	gNodeB
HS	High Speed
HST	High-Speed Train
ICI	Inter-Carrier Interference
IF	Intermediate Frequency
IPDP	Instantaneous Power Delay Profile
ISI	Inter-Symbol Interference
ITU-R	International Telecommunication Union's Radio Communication Sector
LBS	Last Bounce Scatterer
LoS	Line-of-Sight
LS	Least Squares
MFT	Multi-Flow Transmission
MHN	Mobile Hotspot Network
MHN-E	MHN Enhanced
MIMO	Multiple-Input Multiple-Output
MMSE	Minimum Mean-Squared Error
MPC	Multipath Component
MR	Mobile Relay
MT	Mobile Terminal
MWB	Mobile Wireless Backhaul
mDU	Mobile-Backhaul Digital Unit
mm-wave	Millimeter wave
mRU	Mobile-Backhaul Radio Unit
mTE	Mobile-Backhaul Terminal Equipment
NLoS	Non-Line of Sight

The information contained in this document is the property of the contractors. It cannot be reproduced or transmitted to thirds without the authorization of the contractors.



---

**Title:** Deliverable D3.8: Final results on the mobility framework  
**Date:** 31 May 2018      **Status:** Final  
**Security:** Public      **Version:** V1.0

---

NR	New Radio
OLoS	Obstructed Line of Sight
OLSM	Open-Loop Spatial Multiplexing
PDP	Power Delay Profile
PHY	Physical Layer
PPP	Poisson point process
PRACH	Physical Random Access Channel
PUSCH	Physical Uplink Shared Channel
QAM	Quadrature Amplitude Modulation
QCL	Quasi Co-Located
QoS	Quality of Service
QuaDRiGa	QUAsi Deterministic Radlo channel GenerAtor
RMS	Root Mean Square
RAN	Radio Access Network
RLF	Radio Link Failure
RMSI	Remaining Minimum System Information
RRC	Radio Resource Control
RRH	Radio Remote Head
RS	Reference Signal
RSRP	Reference Signal Received Power
RSSI	Received Signal Strength Indicator
RT	Ray Tracer
Rx	Receiver
SAP	Single Antenna Port
SCS	Subcarrier Spacing
SFBC	Space Frequency Block Coding
SFT	Single-Frequency Transmission
SISO	Single-Input and Multiple-Output
SINR	Signal to Interference and Noise Ratio
SNR	Signal-to-Noise Ratio
SRS	Sounding Reference Signal
SSB	Synchronization Signal Block
UE	User Equipment
TA	Timing Advance
TB	Transport Block
TBS	Transport Block Size
TDL	Tapped Delay Line
TM	Transmission Mode
TRP	Transmit/Receive Point
TTI	Transmission Time Interval
Tx	Transmitter
TXD	Transmit Diversity
UL	Uplink
VCA	Virtual Circular Array Antenna
WG	Working Group
WSS	Wide Sense Stationary
XPD	Cross Polarization Discrimination
XPR	Cross-Polarization Radio
ZSA	Zenith Angular Spread of Arrival



---

<b>Title:</b>	Deliverable D3.8: Final results on the mobility framework		
<b>Date:</b>	31 May 2018	<b>Status:</b>	Final
<b>Security:</b>	Public	<b>Version:</b>	V1.0

---

## List of Figures

Figure 1: Channel sounder setup used for measurements.....	10
Figure 2: Map of measurement location with Tx positions and Rx paths .....	11
Figure 3: Fixed transmitter at Tx position 1 .....	12
Figure 4: Mobile receiver on Rx path 1 .....	12
Figure 5: Line-of-sight path loss and fitted model .....	13
Figure 6: CDF of RMS delay spread, logarithmic scaling .....	14
Figure 7: CDF of angle spread .....	14
Figure 8: Transition between segments [7] .....	16
Figure 9: LoS path loss simulated with QuaDRiGa model compared to measurement (Rx path 1) .....	18
Figure 10 Methodology of the performance evaluation of the MHN-E system at 500 km/h ...	19
Figure 11 RMS Delay spreads and Rician K-factors the three straight scenarios.....	20
Figure 12 RMS Delay spreads and Rician K-factors the curved route scenarios.....	21
Figure 13 XPRs of the three straight scenarios .....	21
Figure 14 XPRs of the curved scenarios.....	21
Figure 15 Simulation result for parameter 1 (K-factor=20 dB, XPD=0 dB) .....	23
Figure 16 Simulation result for parameter 2 (K-factor=20 dB, XPD=50 dB) .....	24
Figure 17 Simulation result for parameter 3 (K-factor=13.3 dB, XPD=25 dB) .....	24
Figure 18 Simulation result for parameter 4 (K-factor=7 dB, XPD=0 dB) .....	25
Figure 19 Illustration of simulation parameter setting ( $d_{mRU} = 1000$ m) .....	26
Figure 20 SNR of CIRs versus train location .....	27
Figure 21 Performance of SFT versus mTE 1 location in the x-axis (Instantaneous MCS and TM at 500 km/h) .....	27
Figure 22 Performance of SFT versus mTE 1 location in the x-axis (downlink throughput at 500 km/h).....	28
Figure 23 Downlink throughput of MFT versus mTE 1 location in the x-axis.....	28
Figure 24 CDF of downlink throughput for different velocities of train .....	29
Figure 25 CDF of downlink throughput under 3GPP HST (SFT).....	29
Figure 26: Proposed framework for HST communications [D3.7].....	31
Figure 27: Coverage region for a beamwidth $\theta$ .....	35
Figure 28: SNR coverage probabilities for a threshold of $\gamma = -10$ dB vs the fractional power split for different $\lambda$ .....	36
Figure 29: Beam misalignment error with respect to beamwidth of the transmit antenna.....	36



---

<b>Title:</b>	Deliverable D3.8: Final results on the mobility framework		
<b>Date:</b>	31 May 2018	<b>Status:</b>	Final
<b>Security:</b>	Public	<b>Version:</b>	V1.0

---

Figure 30: Distance estimation error vs physical data rate for different power budget.....	37
Figure 31: Distance estimation error vs physical data rate for different power budget.....	38
Figure 32 Linear deployment architecture for HST .....	39
Figure 33 Coverage probability vs. SNR for different m values .....	41
Figure 34 Spectral efficiency vs. SNR for 3GPP HST channel environemnt.....	44
Figure 35. Example of multiple beams at gNB.....	45
Figure 36. Comparison of NR short preamble formats with reference PUSCH SCS of 15kHz .....	46
Figure 37. Performance comparison with different preamble subcarrier spacing under AWGN and TDL-D channels .....	48
Figure 38. NR HS scenario bidirectional network deployment with 4 GHz carrier frequency.	49
Figure 39. NR HS scenario unidirectional network deployment with 30 GHz carrier frequency .....	49
Figure 40. An example of channel gain (combination of free-space path loss and directional antenna radiation pattern) observed by a moving HST .....	50
Figure 41. Directional network deployment for HST communications with multi-beam operations.....	50



---

<b>Title:</b>	Deliverable D3.8: Final results on the mobility framework		
<b>Date:</b>	31 May 2018	<b>Status:</b>	Final
<b>Security:</b>	Public	<b>Version:</b>	V1.0

---

## 1 Introduction

The objective of this deliverable is to provide the final results on mobility framework, which is of one of the main concerns of the 5G CHAMPION project. More specifically, since the target is to achieve multi-Gbps transmission over very high mobility scenario up to 500 km/h, reliable channel modeling is needed as a prerequisite for evaluating mobility support schemes. Several link-level mobility management schemes are of interest including positioning, random access, handover triggering, and so on.

We first study mmWave channel modeling for high mobility scenario. For accurate and reliable channel modeling, extensive channel measurement campaigns are conducted on an actual railroad environment. Key channel modeling parameters include path loss, RMS delay spread, and RMS azimuth/zenith angle spread of arrival. Based on the extracted actual measurement, channel modeling is done using several tools such as QuaDRiGa and ray tracer. Using the developed channel models, mobility-related functionalities are evaluated in a link-level.

Analysis of mmWave-based beamforming system is also important. Regarding this issue, we analyze the effects of positioning error and beam alignment error on coverage. In addition, fundamental trade-off between distance estimation accuracy and data rate are also investigated.

We also provide coverage analysis which contains the closed-form expression for the coverage probability. It can be useful when determining, for example, inter-RRH distance and transmit power. Nakagami-m fading model is employed so as to reflect various LoS ratio. The link-level performance is also evaluated using the 3GPP 5G NR channel model.

Finally, random access schemes to support initial access and mobility procedure are developed. More specifically, random access preamble formats and handover triggering schemes are investigated in-depth.

This deliverable is organized as follows. We first provide channel modeling issues in Section 2. Then, the analysis on the effects of positioning is discussed in Section 3. Section 4 discusses coverage analysis, link-level evaluation, random access, and mobility support. Section 5 concludes the deliverable.



---

<b>Title:</b>	Deliverable D3.8: Final results on the mobility framework		
<b>Date:</b>	31 May 2018	<b>Status:</b>	Final
<b>Security:</b>	Public	<b>Version:</b>	V1.0

---

## 2 mmWave channel modeling for high mobility

### 2.1 Channel measurement and modeling of a rural 28 GHz HST scenario (HHI)

To accurately model the mmWave communication channels, it is necessary to thoroughly measure the wireless propagation scenario. In this chapter, we present the measurement and modeling of a 28 GHz high speed train (HST) channel in a rural scenario. The measurements were carried out at a freight depot with several train tracks, trees, and buildings. Using a wideband channel sounder setup operating at 28 GHz, the channel was spatially captured both in a large-scale and small-scale manner. A full set of parameters have been extracted to characterize the propagation environment in terms of path loss, delay-related channel parameters, and angle-of-arrival properties as well as parameter correlations and decorrelation distances. The parameter table was then integrated into the QuaDRiGa channel model [7], which has been derived from existing GSCMs such as the WINNER [8] and 3GPP-3D [9] channel model. Both the large and small scale fading parts of the model were extended to overcome drawbacks and limitations of the state-of-the-art approaches, especially in the department of the mobility of MTs. Since the environment can be assumed as being mostly static, the parameters gained from the measurements carried out at low speed can be transferred to high mobility scenarios by scaling the motion speed in the geometry-based stochastic channel model (GSCM).

In 2.1.1, the measurement campaign is introduced with an overview of the channel sounder hardware and a description of the scenario. The parameter extraction process is described in 2.1.2. An overview of the challenges of channel modeling for high mobility scenarios is given in 2.1.3. Finally, in 2.1.4 the parameter table is shown and the extension of the QuaDRiGa channel model for HST communications is described.

#### 2.1.1 Measurement Campaign

The channel measurements were conducted using an advanced instrument-based time domain channel sounder setup depicted in Figure 1. The sounding signal, a periodic Frank-Zadoff-Cho (FZC) sequence, is generated by an FPGA-based signal generator at an intermediate frequency (IF) of 3 GHz with a bandwidth of 933 MHz. A signal duration of 96  $\mu$ s was chosen, leading to an 89,568 element FZC sequence, which yields a processing gain of 49.5 dB. The sounding signal is converted up to 28 GHz ( $\lambda = 10.71$  mm) and fed through a power amplifier with an average power of 34 dBm. It is then transmitted using a vertically polarized omni-directional antenna with a gain of 0 dBi.



<b>Title:</b>	Deliverable D3.8: Final results on the mobility framework		
<b>Date:</b>	31 May 2018	<b>Status:</b>	Final
<b>Security:</b>	Public	<b>Version:</b>	V1.0

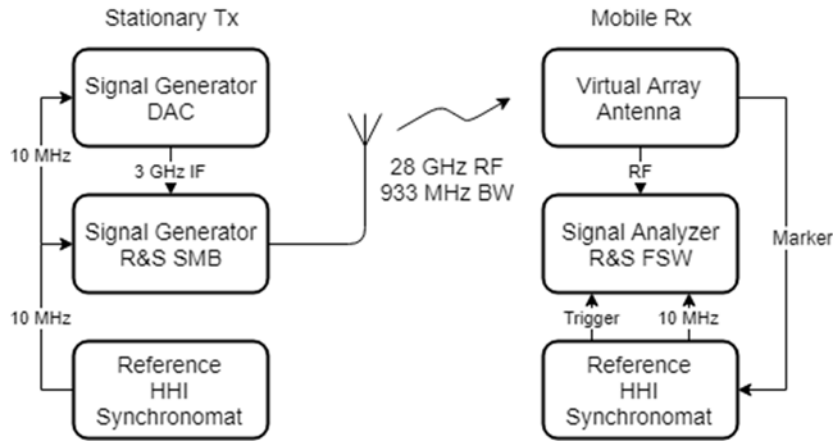


**Figure 1: Channel sounder setup used for measurements**

A virtual circular array antenna (VCA) is used at the receiver side. After the received signal is fed through a low-noise amplifier, it is captured by a signal analyzer with a resolution of 16 bit and stored as base band samples. Synchronization between transmitter (Tx) and receiver (Rx) is achieved by using a high precision rubidium clock, which allows both sides to operate completely independent and also enables coherent triggering of the Rx. Before each measurement, the system is calibrated on site.

The main challenge in generating a channel model for a HST scenario is the measurement campaign necessary to parameterize the wireless propagation channel. Access to railway environments is usually much more restricted than for other rural scenarios. The measurements for this campaign were conducted at a freight depot in Elstal, near Berlin, Germany. Several train tracks run in parallel, limited by trees on either side. Figure 2 shows a map of the measurement location. Both the transmitter (Figure 3) and receiver (Figure 4) were placed on the beds of pick up trucks which were used as measurement vehicles. The antenna heights were chosen to represent a mobile backhaul scenario with the fixed transmitter resting at a height of 5m above ground and the mobile receiver at a height of 3m above ground.



<b>Title:</b>	Deliverable D3.8: Final results on the mobility framework		
<b>Date:</b>	31 May 2018	<b>Status:</b>	Final
<b>Security:</b>	Public	<b>Version:</b>	V1.0

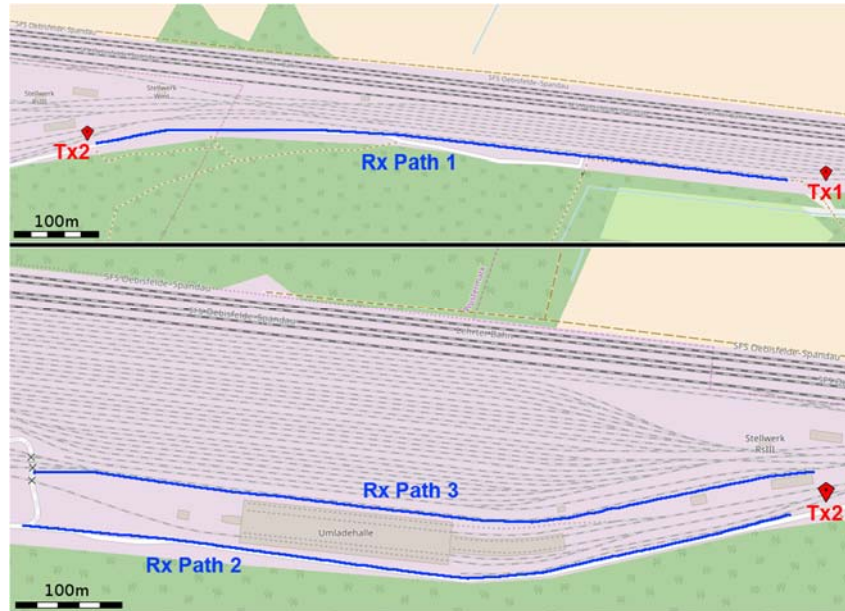


**Figure 2: Map of measurement location with Tx positions and Rx paths**

Two different Tx positions and three Rx paths were used for the measurements. During the measurements on Rx path 1, the transmitter was at Tx position 1. The measurements on Rx paths 2 and 3 were conducted with the transmitter at Tx position 2. On all paths, the minimal distance between transmitter and receiver was 40m. The line of sight was unobstructed on Rx paths 1 and 2, on Rx path 3 the condition was mostly obstructed or non-line-of-sight (OLoS/NLoS).

On each Rx path, two different types of measurements were conducted. The large scale effects were captured by moving the receiver at a constant speed of 1.75 m/s for a distance of up to 850 m. During each measurement, 5000 channel impulse response (CIR) snapshots were captured, resulting in one CIR snapshot every 17.5 cm. The VCA was fixed during the large scale measurements and acted as a simple vertical dipole. The angles of arrival (AoA) were captured at 20m intervals at fixed positions on each path using the rotating VCA. During these measurements, 1000 CIR snapshots corresponding to the 1000 virtual array elements were taken for each position.



---

<b>Title:</b>	Deliverable D3.8: Final results on the mobility framework		
<b>Date:</b>	31 May 2018	<b>Status:</b>	Final
<b>Security:</b>	Public	<b>Version:</b>	V1.0

---



*Figure 3: Fixed transmitter at Tx position 1*



*Figure 4: Mobile receiver on Rx path 1*

### 2.1.2 Parameter Extraction

Power delay profiles (PDP) were derived from the CIRs captured by the channel sounder in order to extract the parameters for the channel model. In the PDPs, the multipath components (MPC) were identified, whereas MPCs with a power less than the PDP's median plus an *absolute threshold* of 13 dB are discarded as noise. The so-called instantaneous power delay profiles (IPDP) were calculated based on the large-scale measurements while the 1000 PDPs for each AoA measurement position were averaged into so called averaged power delay profiles (APDP). Based on the IPDPs and APDPs, statistical parameters have been extracted. An in-depth explanation of the measurement data processing and parameter extraction is in [1]. For the parameter extraction, only the data from Rx paths 1 and 2 in pure



<b>Title:</b>	Deliverable D3.8: Final results on the mobility framework		
<b>Date:</b>	31 May 2018	<b>Status:</b>	Final
<b>Security:</b>	Public	<b>Version:</b>	V1.0

line of sight condition was taken into account. On Rx path 1 this was from 40 to 550m, on Rx path 2 from 40 to 350m.

### 2.1.2.1 Path Loss

A path loss model was derived using a linear least squares fit to the data from the large-scale measurements. The cumulated power of the MPCs was averaged over six consecutive IPDPs in order to minimize small-scale fading effects. A path loss model was then fitted based on the data in pure LoS condition. The resulting path loss exponent and shadow fading parameter are given in Table 1, where  $\bar{L}_{PL}(d_0)$  is the mean path loss at the reference distance  $d_0$ . In accordance with the model, the mean path loss at the reference distance was set to be equal to the free space path loss (FSPL). The LoS path loss, fitted model, and FSPL are illustrated in Figure 5.

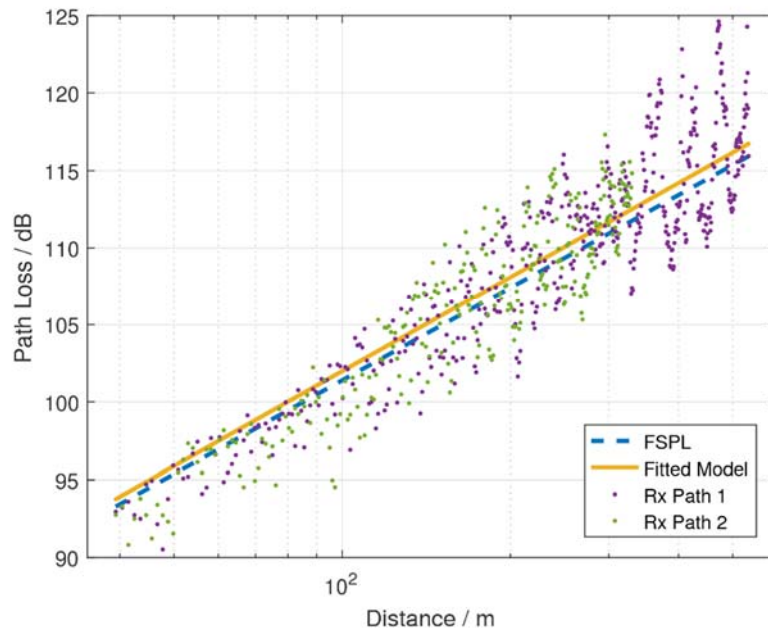


Figure 5: Line-of-sight path loss and fitted model

### 2.1.2.2 RMS Delay Spread

For the calculation of the root mean square (RMS) delay spread ( $D_s$ ), a relative evaluation threshold of 30 dB to the IPDPs of Rx paths 1 and 2 in LoS condition. The cumulative distribution function (CDF) of the RMS DS on a logarithmic scale together with the fitted model is shown in Figure 6. The statistical parameters are given in Table 1.



**Title:** Deliverable D3.8: Final results on the mobility framework  
**Date:** 31 May 2018 **Status:** Final  
**Security:** Public **Version:** V1.0

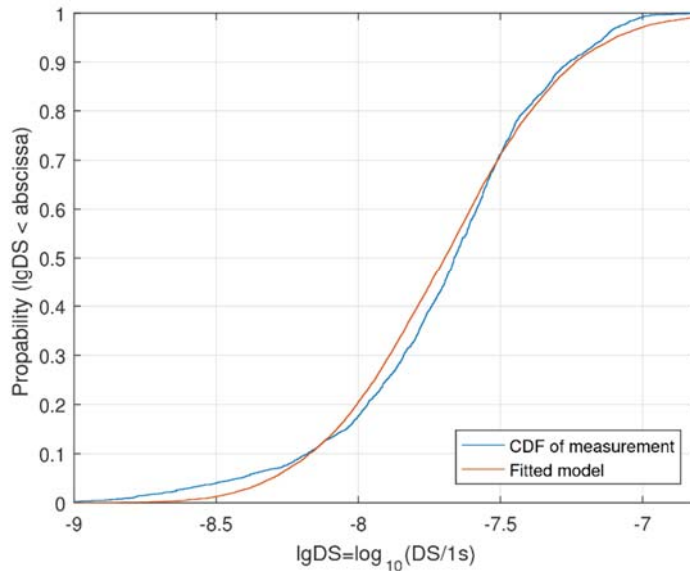


**Figure 6: CDF of RMS delay spread, logarithmic scaling**

### 2.1.2.3 RMS Azimuth / Zenith Angle Spread of Arrival

The RMS angle spreads of arrival in both azimuth (ASA) and zenith (ZSA) were estimated based on the AoA measurements conducted using the VCA. Similar to the RMS delay spread, an evaluation threshold of 30 dB was applied on the data from Rx paths 1 and 2 in LoS condition. The CDF of the RMS ASA and ZSA is shown in Figure 7. Again, the statistical parameters are given in Table 1.

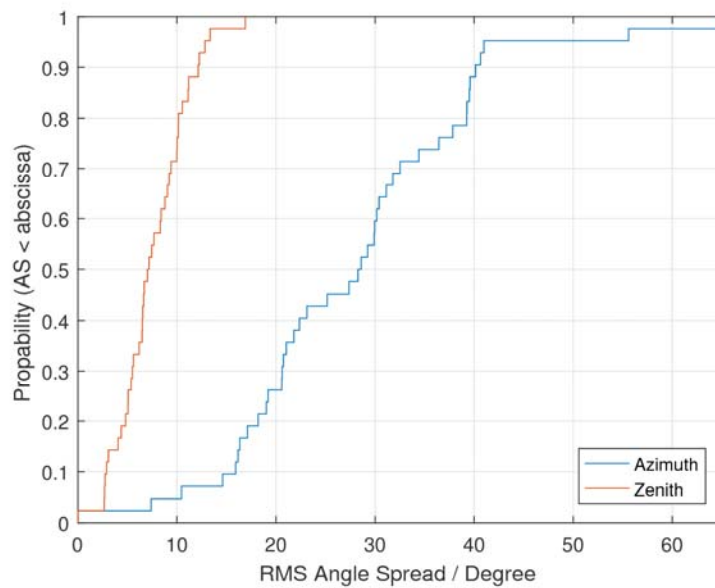


**Figure 7: CDF of angle spread**

The information contained in this document is the property of the contractors. It cannot be reproduced or transmitted to thirds without the authorization of the contractors.



---

<b>Title:</b>	Deliverable D3.8: Final results on the mobility framework		
<b>Date:</b>	31 May 2018	<b>Status:</b>	Final
<b>Security:</b>	Public	<b>Version:</b>	V1.0

---

### 2.1.3 Channel Modelling for High Mobility

Continuous time evolution of channel traces is the most challenging aspect of channel modeling for high mobility. In one approach for short-term time evolution, which was added to 3GPP-SCM by Xiao et al. [2], the positions of the last-bounce scatterers (LBS) are calculated based on the arrival angles of individual MPCs. Delays and phases are updated upon movement of the mobile terminal (MT). Most channel models, however, do not incorporate this technique, therefore limiting the mobility of MTs to just a few meters. Another approach is considered by the COST model [3]. Groups of randomly placed so-called scattering clusters are introduced. These clusters fade in and out depending on the position of the MT. A simplified version of this method was presented by Czink et al. [4] where clusters fade in and out over time. This concept led to further research on the birth and death of scattering clusters [5] and a model for non-stationary channels by Wang et al. [6] that allows the scattering clusters to be mobile.

QuaDRiGa [7] is a channel model that has been derived from existing GSCM such as the WINNER [8] and 3GPP-3D [9] model at Fraunhofer HHI. It supports time evaluation and 3D propagation effects. The large and small scale fading parts of the model were extended in several ways to support highly mobile MTs. Two key aspects in this are *drifting* and *transition between segments*.

#### 2.1.3.1 Drifting

To ensure spatial consistency, the path delays, powers, and angles need to be constantly updated when the MT moves to a different location. When this is not done, the channel coefficients at the output of the channel model do not agree well with the reality. A simplified approach is used by most state-of-the-art GSCMs like the 3GPP-3D [9] model. Each MPC gets assigned a Doppler shift based on the initial arrival angles, but the angles and path delays remain unchanged. Additionally, the movement of an MT cannot be explicitly modeled and is assumed to be with a constant speed in a fixed direction. With QuaDRiGa, the user can specify a trajectory along which the MT moves. This trajectory is then divided into several meters long segments. It is assumed that the wide sense stationary (WSS) properties of the channel remain more or less constant for the time it takes the MT to traverse through the segment. At the edge of each segment, the birth and death of MPCs is treated. By updating the path parameters like delay, angles, and phases for each MT position along the segment, a continuous time evolution is incorporated.

#### 2.1.3.2 Transition between Segments

Of course, scatterer positions are not fixed and the channel is only WSS for a short path of the MT trajectory. Whenever the MT moves over a larger distance, the large scale parameters will change because the MT will see different scattering clusters. In order to be able to support longer MT trajectories, the channel model therefore needs to handle the *birth and death* of scattering clusters. In QuaDRiGa, the power of paths in adjacent segments are ramped up and down, therefore keeping the large scale parameters consistent. The large scale parameters are reasonably constant within each segment. Independent scattering clusters, channel coefficients, and path delays are generated for each segment using the small scale fading model. Two adjacent segments overlap as displayed in Figure 8. The *birth and death* of scattering clusters is handled by ramping down the power of paths from the old segment and ramping up the power of the new paths during the overlapping part of the segments.



<b>Title:</b>	Deliverable D3.8: Final results on the mobility framework		
<b>Date:</b>	31 May 2018	<b>Status:</b>	Final
<b>Security:</b>	Public	<b>Version:</b>	V1.0

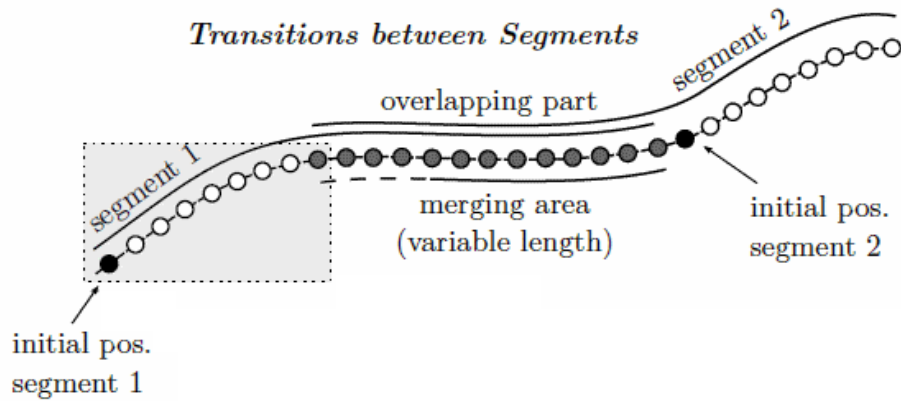


Figure 8: Transition between segments [7]

### 2.1.3.3 Modeling of Velocity

In HST scenarios, the propagation is mainly influenced by the environmental scatterers. In the considered scenario, those scatterers are mostly static objects like buildings or trees. The environment can therefore be assumed as static. The velocity of the MT in this case can be taken into account in the channel model independently of the measurement velocity. GSCMs like QuaDRiGa model the position of the MT as a function of time, therefore the velocity is indirectly accounted for in the channel model. As long as the environment is parameterized thoroughly, any given velocity of the MT can be modeled. For the presented channel model, an extensive measurement campaign in a railway scenario was conducted. Both large scale parameters and angle of arrivals of the channel were captured. Based on this data, QuaDRiGa is able to generate accurate channel impulse responses for any arbitrary velocity.

### 2.1.4 QuaDRiGa-based Channel Model

Using the parameters extracted from the measurement data, the QuaDRiGa channel model was extended to support rural HST scenarios. As a validation for the extension, the trajectory of the LoS part of Rx path 1 was parameterized as a QuaDRiGa track and a set of contiguous random channels was generated. The path loss was then compared to the measurement data.

Table 1 gives an overview over the parameters used to extend the channel model. Besides the large scale parameters delay spread, shadow fading, and K-Factor, decorrelation distances and cross correlations between the parameters were calculated. The very short decorrelation distances of the K-factor and shadow fading can be explained by small-scale fading effects like ground reflection, whose MPCs are not resolvable with the used measurement bandwidth. The decorrelation distances for the AoA parameters could not be calculated because the distance between measurement points was larger than the expected decorrelation distance. The parameters that could not be estimated were substituted with values from the 3GPP TR38.901 [10] Urban Macro (UMa) channel model. Although the *Rural Macro* model may seem more appropriate for this scenario, it only applies to frequencies up to 7 GHz. Comparison between the parameters extracted from the measurements and the 3GPP model show that the values of the HST scenario are smaller, but of the same order of magnitude as the 3GPP UMa parameters.



**Title:** Deliverable D3.8: Final results on the mobility framework  
**Date:** 31 May 2018 **Status:** Final  
**Security:** Public **Version:** V1.0

Parameter		HST Rural	3GPP UMa
Delay Spread (DS) $\lg_{DS} = \log_{10}(DS/1s)$	$\mu_{\lg_{DS}}$	-7.70	-7.01
	$\sigma_{\lg_{DS}}$	0.37	0.66
AOA Spread (ASA) $\lg_{ASA} = \log_{10}(ASA/1^\circ)$	$\mu_{\lg_{ASA}}$	1.42	1.81
	$\sigma_{\lg_{ASA}}$	0.19	0.20
ZOA Spread (ZSA) $\lg_{ZSA} = \log_{10}(ZSA/1^\circ)$	$\mu_{\lg_{ZSA}}$	0.084	0.095
	$\sigma_{\lg_{ZSA}}$	0.21	0.16
Path Loss (PL) $d_0 = 1m$	$n$	2.03	-
	$\bar{L}_{PL}(d_0)$	61.4	-
Shadow Fading (SF) [dB]	$\sigma_{SF}$	2.8	4
K-factor (K) [dB]	$\mu_K$	8.51	9
	$\sigma_K$	4.78	3.5
Cross-Correlations	DS vs SF	0.2	-0.4
	DS vs K	-0.1	-0.4
	SF vs K	-0.6	0.5
Decorrelation distance [m]	DS	16	30
	SF	2	37
	K	2	12

**Table 1: Channel model parameter table**

In Figure 9, a comparison between the LoS path loss of a channel generated using the QuaDRiGa model and the measurement on Rx path 1 is shown. The gradients of the generated and measured channel are very similar. Further comparison of the generated channel data has shown that the QuaDRiGa model generates valid channels that agree well with the measurement results.



<b>Title:</b>	Deliverable D3.8: Final results on the mobility framework		
<b>Date:</b>	31 May 2018	<b>Status:</b>	Final
<b>Security:</b>	Public	<b>Version:</b>	V1.0

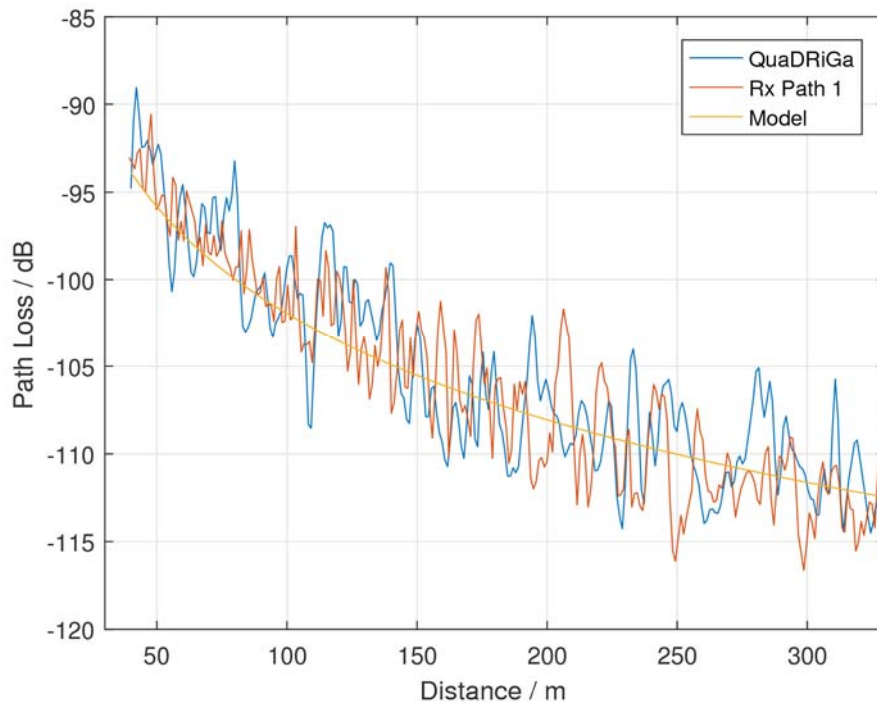


Figure 9: LoS path loss simulated with QuaDRiGa model compared to measurement (Rx path 1)

## 2.2 MHN-E channel measurement and modeling (ETRI)

Due to the unavailability of a real HST running at a speed of up to 500 km/h, it is hard to evaluate the performance of the MHN-E system at this speed through a real field trial with a bus. Hence, channel models for various HST scenarios with mobility of up to 500 km/h were studied first. Then, as shown in Figure 10, a joint simulation between those channel models and the MHN link-level simulator was conducted to validate the performance of the MHN-E system at a speed of up to 500 km/h as an alternative to a field trial at 500 km/h. In the simulation, the parameter settings are identical to the testbeds used for the bus demonstration.

Following are the two channel models studied for the joint simulation.

- Ray-tracing-based channel model
  - ✓ Multipath-cluster channel model with Rician fading based on ray-tracer calibration with measurement results
- QuaDRiGa-based channel model
  - ✓ QuaDRiGa-based channel model developed by parameters extracted from the measurement campaign



**Title:** Deliverable D3.8: Final results on the mobility framework  
**Date:** 31 May 2018 **Status:** Final  
**Security:** Public **Version:** V1.0

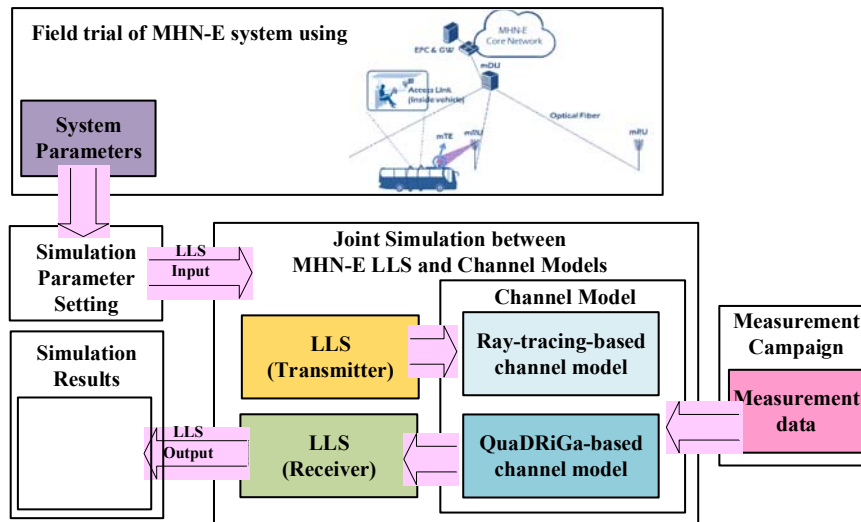


**Figure 10** Methodology of the performance evaluation of the MHN-E system at 500 km/h

The above channel models are developed based on real measurement data. Although measurements will not be conducted in a real 500km/h environment, it is reasonable to claim that these channel models for HST scenarios (500 km/h), which are derived from static measurements, are sufficient to validate the system performance due to rationales described as follows:

- The propagation in the considered HST scenario is mainly influenced by the environment; therefore, the goal of the measurements (by HHI) is to capture scatterers and effects like shadowing and reflections. In typical HST scenarios, the main influencing objects in the environment are static objects like buildings and trees. Therefore, the environment can be assumed static. In this case, the velocity of the train can be taken into account in the channel model independent of the measurement velocity. The channel model could even be derived from static measurements.
- GSCM, like QuaDRiGa, model the position of the mobile entity as a function of time, thus the velocity is indirectly accounted for in the channel model. Any given velocity of the mobile entity can be modeled, as long as the environment is parameterized thoroughly. HHI has done an extensive measurement campaign in a railway scenario in order to capture both large scale parameters and small scale characteristics. These parameters will be included in the QuaDRiGa channel model generator, which will provide an accurate channel model for HST scenarios.
- The influence of the mobility to the channel is composed of two independent factors: multipath environment and speed. In ray-tracing simulations, the rays at one position are determined by the environment at that moment. When the time sampling rate is constant (which is true for the same target communication system), different mobile speeds just result in different sampling positions with the corresponding rays. Thus, if the 3D environment model and propagation mechanism models in the RT are validated by the measurement data at one speed (no matter which is high or low), the RT will be capable to realize the channels at various speeds by generating the rays in the snapshots at corresponding sampling positions.



<b>Title:</b>	Deliverable D3.8: Final results on the mobility framework		
<b>Date:</b>	31 May 2018	<b>Status:</b>	Final
<b>Security:</b>	Public	<b>Version:</b>	V1.0

To summarize, both the RT and GSCM (which can be treated as simplified ray-tracer) are capable to realize realistic channel at higher speed if they are validated at lower speed in the same environment. The speed of mobility just determines the “zoom” scale of channel characteristic curves in both time and frequency domain in a continuous scenario [1].

### 2.2.1 Multipath-cluster channel model with Rician fading (ETRI)

According to the literature [12], propagation characteristics of 27.4 GHz have been investigated that delay spread varies from 21.75 to 75.75 ns, not exceeding 100 ns. In the paper, Soma also claims that the K-factor of Rician fading K, which refers to the ratio of the energy in the LoS path to the energy in the scattered paths, is smaller than 10 dB [12]. However, we believe that the K-factor in the HST scenario is much larger than that due to its unique environment that has scarce reflectors and scatters. Besides, since the mRUs and mTE use very narrow beams for Tx/Rx BF, it may further increase the K-factor and alleviate various effects of the multipath signals including ICI and ISI.

In order to verify our observations on the channel characteristics in HST communications mentioned above and to develop a proper channel model for the simulation, we first conducted a very comprehensive study to investigate the channel characteristics of the MHN-E system in three scenarios of HST communications (urban, rural, tunnel) [13]. In [13], based on the wideband measurements conducted in the tunnel scenario by using the MHN system, a 3-D RT is calibrated and validated to explore more channel characteristics in different HST scenarios. Through extensive RT simulations with 500 MHz bandwidth centered at 25.25 GHz, the power contributions of the multipath components are studied, and the dominant reflection orders are determined for each scenario. In this study, path loss is analyzed, and other key parameters, such as Doppler shifts, RMS delay spread, K-factor, polarization ratios, and so on, are studied.

Then, by referring to the literature [14], we developed a multipath-cluster channel model. The basic observation of the model is that multipath components of clusters, formed by multiple reflections from the objects in the vicinity of Rx and Tx, arrive at Rx in groups. More specifically, a multipath-cluster channel model with Rician fading formed by two clusters is developed based on the key channel parameters observed in the above study. The key channel parameters we take into account in the channel model are RMS delay spread, K-factor, XPR/XPD.

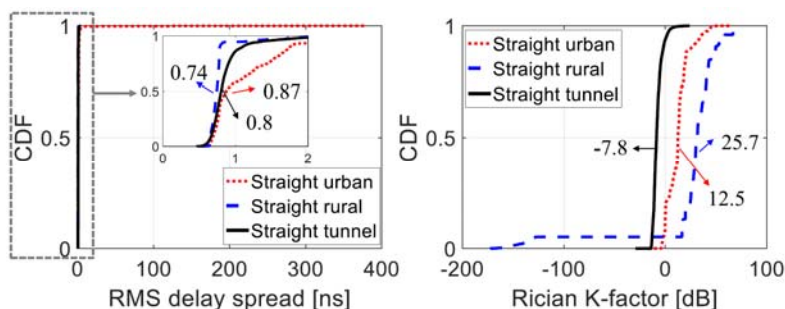
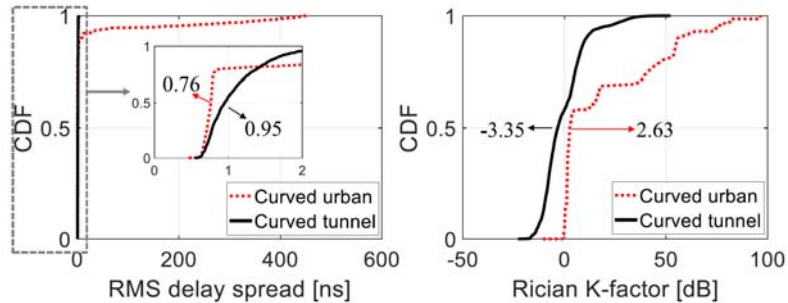


Figure 11 RMS Delay spreads and Rician K-factors the three straight scenarios



**Title:** Deliverable D3.8: Final results on the mobility framework  
**Date:** 31 May 2018 **Status:** Final  
**Security:** Public **Version:** V1.0



**Figure 12** RMS Delay spreads and Rician K-factors the curved route scenarios

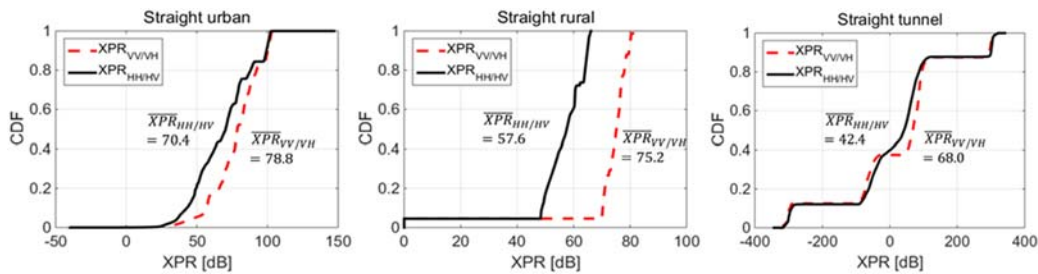


**Figure 13** XPRs of the three straight scenarios

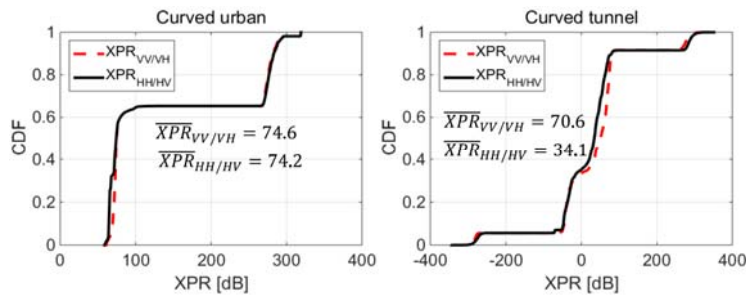


**Figure 14** XPRs of the curved scenarios

Based on our RT simulation results for those parameters as shown in Figure 11~Figure 14, we carefully chose the value of each parameter, and the developed multipath-cluster channel model takes those parameters as input. In the case of RMS delay spread, the RT simulation results showed that the values for three scenarios are less than 2 ns, which is far smaller than we expected. Therefore, considering the Soma's claim that the delay spread varies from 21.75 to 75.75 ns, not exceeding 100 ns, we assumed the worst case that the maximum RMS delay spread is equal to 100 ns, and the total power ratio of primary path to secondary path is 10 dB.

### 2.3 Link-level performance evaluation of MHN-E system for high-speed train communications (ETRI)

Link-level simulation has been conducted to verify the feasibility of the MHN-E system for high mobility of up to 500 km/h under the two channel models described in the previous

The information contained in this document is the property of the contractors. It cannot be reproduced or transmitted to thirds without the authorization of the contractors.



<b>Title:</b>	Deliverable D3.8: Final results on the mobility framework		
<b>Date:</b>	31 May 2018	<b>Status:</b>	Final
<b>Security:</b>	Public	<b>Version:</b>	V1.0

subsection. The performance evaluation mainly focuses on the downlink PHY throughput  $R_{PHY}$ , and spectral efficiency  $C_{PHY}$ , of the MHN-E system, which can be respectively formulated as the following equations,

$$R_{PHY} = \frac{N_{CC}}{T} \cdot \sum_{b \in B(T)} \frac{S_{TB}(b) \cdot (1 - E_{TB}(b))}{T_{TTI}},$$

$$C_{PHY} = \frac{R_{PHY}}{W_{CC} \cdot N_{CC}} = \frac{1}{T \cdot W_{CC}} \cdot \sum_{b \in B(T)} \frac{S_{TB}(b) \cdot (1 - E_{TB}(b))}{T_{TTI}},$$

where  $T_{TTI}$  and  $N_{CC}$  denote TTI and the number of CCs respectively, and  $B(T)$  represents a set of TBs transmitted by an mRU using one CC during a certain duration of  $T$ .  $S_{TB}(b)$  is the TBS of  $b$ -th TB and  $E_{TB}(b)$  stands for its TB error indicator, which is equal to 1 if block error has occurred and otherwise, is equal to 0.

### 2.3.1 Link-level simulation under multipath-cluster channel model

#### Simulation Assumptions:

The simulation parameters are listed in Table 2 and performance evaluations mainly focus on PHY spectral efficiency of the system. By varying the K-factors of Rician fading and XPD based on the observations from Figure 11~Figure 14, we would like to implement multipath-cluster channel models with Rician fading that mirror various scenarios such as rural and tunnel environments. As summarized in Table 2, K-factor of 20 dB and two K-factors of 13.3 dB and 7 dB, which are being considered for performance evaluation of a HST scenario in 3GPP [15][16] were considered. In addition, three different values of XPD, 0 dB, 25 dB, and 50 dB were taken into account. In the simulation, frequency offset due to the Doppler effect was compensated at the receiver using AFC [17].

**Table 2 Simulation Parameters**

Parameters	Set 1	Set 2	Set 3	Set 4
Channel model	Multipath-cluster channel model with Rician fading channel			
K-factor (dB)	20	20	13.3	7
XPD (dB)	0	50	25	0
RMS delay spread (ns)	100	100	100	100
Carrier frequency (GHz)	26			
Velocity (km/h)	100, 300, 500			
Code rate	0.8			
Modulation order	QPSK, 16-QAM, 64-QAM			
Transmission scheme	2x2 MFT			
TM for each mTE	TM1, TM2	TM3	TM2, TM3	TM2, TM3
Number of mTE antennas	2			
Number of mRU antennas	1 for TM1 2 for TM2	2	2	2
Receiver	AFC for Doppler compensation, Turbo decoder			

**TM1:** SAP transmission (SISO), **TM2:** SFBC-based TXD, **TM3:** OLSM



<b>Title:</b>	Deliverable D3.8: Final results on the mobility framework		
<b>Date:</b>	31 May 2018	<b>Status:</b>	Final
<b>Security:</b>	Public	<b>Version:</b>	V1.0

### Simulation results for parameter 1 and 2:

As shown in Figure 15, it is observed that, as the velocity increases, the performance degrades due to the ICI caused by Doppler effect. As expected, the TM2 gives better performance owing to diversity gain. Although we omitted the performance of TM3 in Figure 15, it actually turns out that the TM3 cannot provide performance gain against the TM2 in this channel environment due to the small XPD of 0 dB. Under this channel environment, the system running at 500 km/h is able to achieve average spectral efficiency of up to 3.61 bps/Hz using TM2 and 16-QAM.

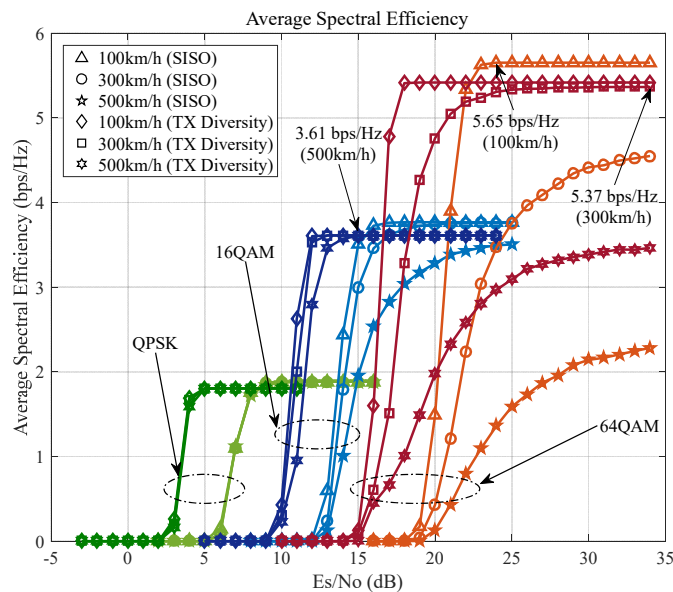


Figure 15 Simulation result for parameter 1 ( $K$ -factor=20 dB,  $XPD=0$  dB)

Figure 16 showed that in the case of channel with large XPD of 50 dB, the MHN-E system using TM3 (2x2 OLSM transmission scheme) is able to achieve average spectral efficiency of up to 10 bps/Hz when the SNR is larger than 25 dB and the moving speed is less than 100 km/h. In the case of 500 km/h, the MHN-E system is able to achieve average spectral efficiency of up to 6.41 bps/Hz using TM3 and 16-QAM, indicating that at a very high speed like 500 km/h, using a lower modulation order such as 16-QAM may be more suitable.



**Title:** Deliverable D3.8: Final results on the mobility framework  
**Date:** 31 May 2018 **Status:** Final  
**Security:** Public **Version:** V1.0

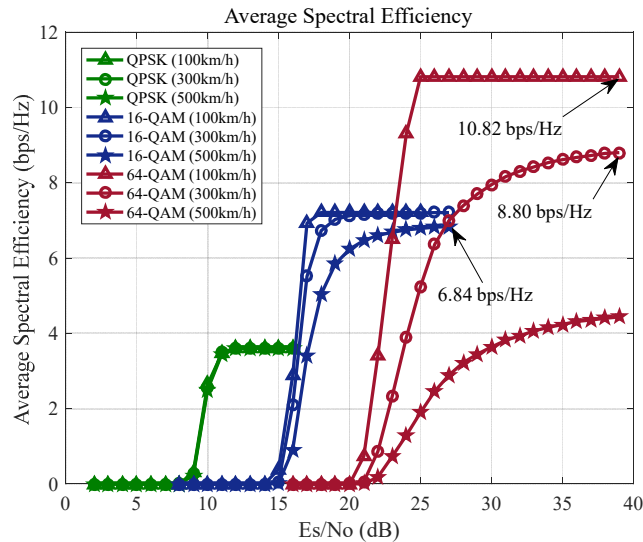


Figure 16 Simulation result for parameter 2 ( $K$ -factor=20 dB,  $XPD$ =50 dB)

**Simulation results for parameter 3 and 4:**

The link-level simulation result in Figure 17 shows that in the case of the channel with a  $K$ -factor of 13.3 dB and  $XPD$  of 25 dB, the system using the TM3 (2x2 OLSM) is able to achieve better spectral efficiency performance than that of TM2 (2x2 TXD) most of the time. When the velocity of the train is 100 km/h or 300 km/h, the system using 64-QAM with TM3 can achieve spectral efficiency exceeding 9 bps/Hz, while a maximum spectral efficiency of 6 bps/Hz at the speed of 500 km/h can be achieved using 16-QAM with TM3 at SNR larger than 30 dB. From this simulation result, we can draw a conclusion that under a channel environment with a dominant LoS path and large  $XPD$  like a rural environment, the OLSM transmission scheme is preferred, to increase the spectral efficiency.

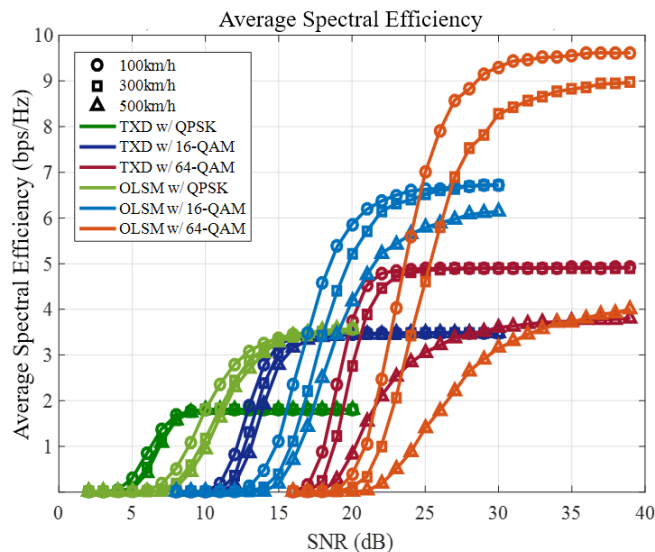


Figure 17 Simulation result for parameter 3 ( $K$ -factor=13.3 dB,  $XPD$ =25 dB)

The information contained in this document is the property of the contractors. It cannot be reproduced or transmitted to thirds without the authorization of the contractors.



However, it is observed in the other simulation result as shown in Figure 18 that in the case of the channel with a K-factor of 7 dB and XPD of 0 dB, only the TM2 (2x2 TXD) yields reasonable spectral efficiency performance, while the TM3 (2x2 OLSM) is unable to provide performance gain on spectral efficiency. It means that under a channel that has a weak LoS path and small XPD due to large multi-path components, like in tunnel environments, the TXD transmission scheme is preferred.

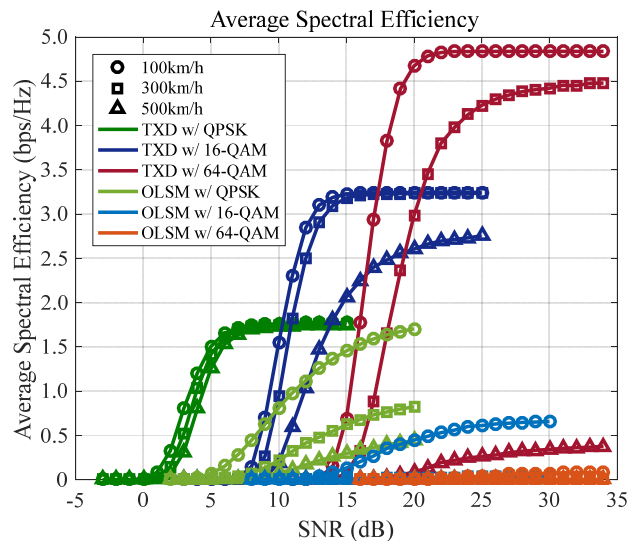


Figure 18 Simulation result for parameter 4 (K-factor=7 dB, XPD=0 dB)

### 2.3.2 Link-level simulation under QuaDRiGa-based channel model

Link-level simulation has been further conducted to evaluate the performance of the MHN-E system under the QuaDRiGa-based channel model, mainly focusing on PHY throughput. In the simulation, an instantaneous throughput is calculated by taking the average of throughputs accumulated every 0.1 m while an average throughput is the average value of throughputs accumulated every 1 m.

#### Simulation Assumptions:

In the simulation, as shown in Figure 19, a total of three mRUs (mRU #1, #2, #3) and two mTEs (mTE #1, #2) were considered for the purpose of evaluating the performance of the MFT technology in the MHN-E system. In this simulation, it is assumed that mRU #1, mRU #2, mRU #3 are located at  $(-d_{mRU}, 5, 5)$ ,  $(0, 5, 5)$ ,  $(d_{mRU}, 5, 5)$  respectively, where  $d_{mRU}$  represents the inter-mRU distance, and a HST carrying mTE 1 and mTE 2 moves along the x-axis. We also assumed that the mTE 1 and mTE 2 respectively start from the coordinates of  $(-200, 0, 3)$  and  $(0, 0, 3)$ , and move to  $(-200+d_{mRU}, 0, 3)$  and  $(d_{mRU}, 0, 3)$ . In this case, the mTE 1 communicates with mRU 3, and the mTE 2 first communicates with mRU 1, and switch to the next mRU (mRU 2) when passing by the mRU 2. Detailed parameters are listed in Table 3.

Table 3 Simulation Parameters

Parameter	Value
Carrier frequency (GHz)	25



**Title:** Deliverable D3.8: Final results on the mobility framework  
**Date:** 31 May 2018 **Status:** Final  
**Security:** Public **Version:** V1.0

System bandwidth (GHz)	1
TX power (dBm)	20
Noise figure (dB)	7
Noise spectral density (dBm/Hz)	-174
Implementation loss (dB)	2
mRU height (m)	5
mTE height (m)	3
Distance between Railway track and mRUs (m)	5
Distance between two mTEs (m)	200
Distance between adjacent mRUs, $d_{mRU}$ (m)	1000, 580
Transmission scheme	SFT, MFT
Number of TX antennas	2
Number of RX antennas	2
TM	TM2 : TXD TM3 : OLSM
Channel estimation	LS estimation
Velocity (km/h)	100, 300, 500
TDD configuration	DSUDDDDD
Number of CCs	8
Equalizer	Alamouti decoder for TXD MMSE equalizer for OLSM
Decoder	Turbo decoder

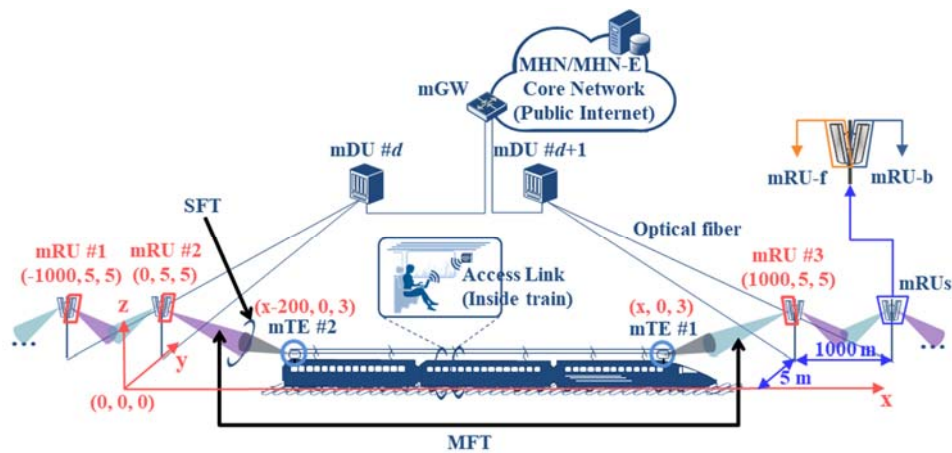


Figure 19 Illustration of simulation parameter setting ( $d_{mRU} = 1000$  m)

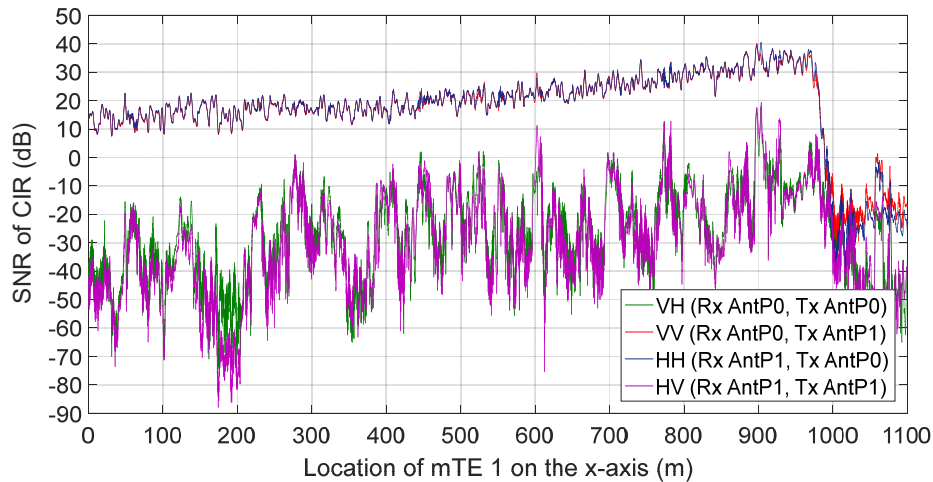
### Simulation Results:

Figure 20 shows an example of the SNR of CIRs generated by QuaDRiGa, which is used as input to the link-level simulator. As shown in Figure 20, owing to the dual-polarized antennas used at the mRU and mTE in the rural HST scenario where the LoS path is dominant XPDs larger than 20 dB are observed at most of the locations along the track, which is highly beneficial to support the OLSM increasing spectral efficiency.

The information contained in this document is the property of the contractors. It cannot be reproduced or transmitted to thirds without the authorization of the contractors.



**Title:** Deliverable D3.8: Final results on the mobility framework  
**Date:** 31 May 2018 **Status:** Final  
**Security:** Public **Version:** V1.0



**Figure 20 SNR of CIRs versus train location**

With the CIRs for 500 km/h, as shown in Figure 21, we first evaluated the performance of SFT between the mTE 1 and mRU 3 by plotting the instantaneous downlink TM, MCS and corresponding downlink throughputs versus mTE location. In Figure 21, we can simply observe that in almost all locations, the TM3 (OLSM) is used rather than the TM2 (SFBC), indicating that the dual-polarized antennas of the MHN-E are capable of efficiently increasing the spectral efficiency in the rural HST scenario. Furthermore, as the HST moves close to the mRU, the path loss decreases gradually, and the MCS index thus increases accordingly. Consequently, as shown in Figure 22, the downlink throughput increases until the mTE passes by the mRU and reaches a peak data rate of 5.68 Gbps with the TM of OLSM and MCS 23 (64-QAM with 0.8887) when the distance between mTE 1 and mRU 3 is around 30 m.

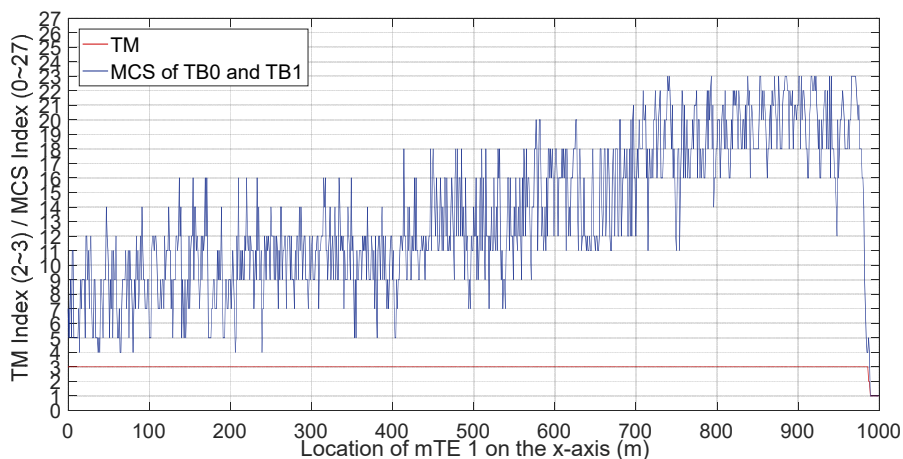


**Figure 21 Performance of SFT versus mTE 1 location in the x-axis (Instantaneous MCS and TM at 500 km/h)**



**Title:** Deliverable D3.8: Final results on the mobility framework  
**Date:** 31 May 2018 **Status:** Final  
**Security:** Public **Version:** V1.0

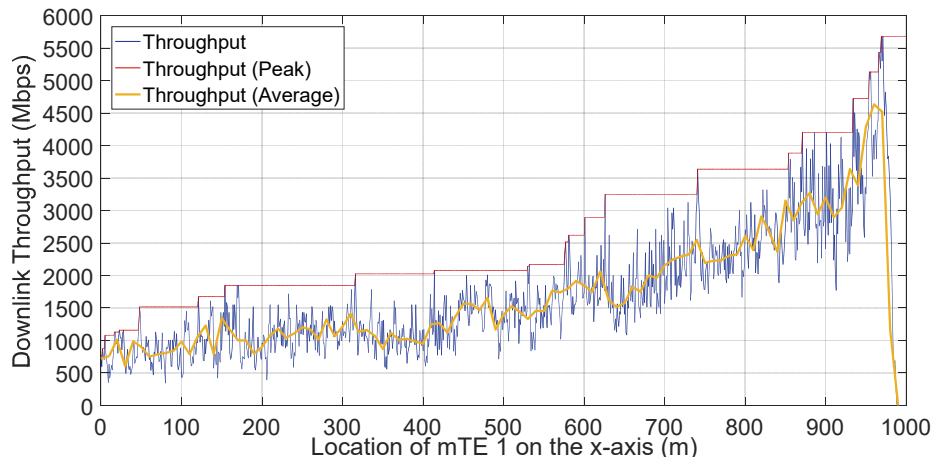


**Figure 22 Performance of SFT versus mTE 1 location in the x-axis (downlink throughput at 500 km/h)**

In addition, we evaluated the performance of the MFT at a speed of 500 km/h. As shown in Figure 23, it was revealed that average throughputs between 3 Gbps and 5.5 GHz can be achieved and a peak can reach up to 6.66 Gbps at the mTE 1 location of 250 m and 970 m in the x-axis. Moreover, it was also shown that the MFT technology can effectively overcome the severe performance degradation of the SFT at the mTE 1 location of around 980 m where the mTE 1 pass by the mRU 3.

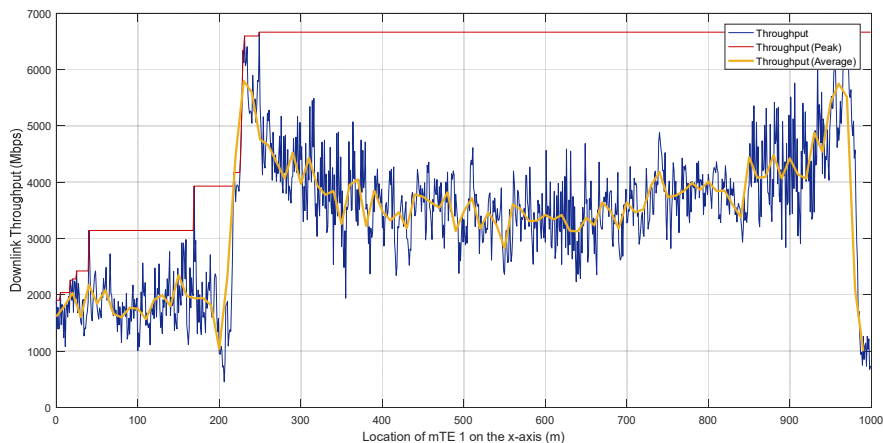


**Figure 23 Downlink throughput of MFT versus mTE 1 location in the x-axis**

Lastly, to compare the downlink data rates of SFT and MFT for the different velocities of mTE, we plotted the CDF of data rates for 100 km/h, 300 km/h and 500 km/h as shown in Figure 24. It is obvious that, as the velocity increases, a slight performance degradation has occurred due to the ICI, but the MHN-E system is still able to provide multi-Gigabit MWB link to a HST at a speed of 500 km/h, which is sufficient for a number of passengers in a HST to access onboard mobile Internet services. In addition, as observed in Figure 25, better performance can be achieved under the 3GPP above-6 GHz HST scenarios [15], where the inter-mRU distance of 580 m is defined. This is obviously due to the fact that both mTE 1 and 2 can



**Title:** Deliverable D3.8: Final results on the mobility framework  
**Date:** 31 May 2018 **Status:** Final  
**Security:** Public **Version:** V1.0

receive larger signal power owing to the reduced communication distance between the mTE and mRU, which has positive impact on the throughput improvement.

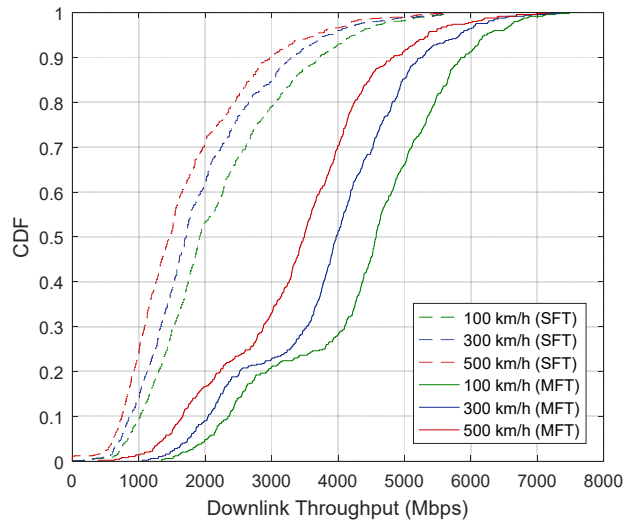


**Figure 24 CDF of downlink throughput for different velocities of train**

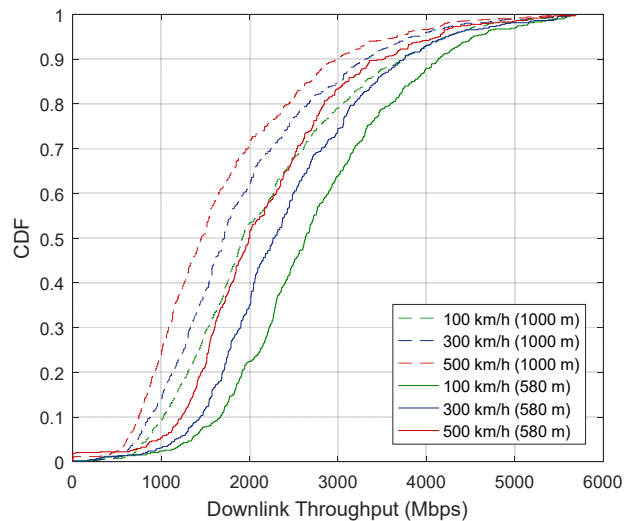


**Figure 25 CDF of downlink throughput under 3GPP HST (SFT)**

**User-experienced data rate in high mobility scenario:**

According to ITU-R requirements for IMT-2020, user-experienced data rate is defined as the 5% point of the CDF of the user throughput, with the target values of 100 Mbit/s for the downlink and 50 Mbit/s for the uplink. The rationale behind this 5th percentile user data rate is to measure the user-experienced QoS for the cell-edge users, assuming traditional two-dimensional cellular networks.

The information contained in this document is the property of the contractors. It cannot be reproduced or transmitted to thirds without the authorization of the contractors.



---

<b>Title:</b>	Deliverable D3.8: Final results on the mobility framework		
<b>Date:</b>	31 May 2018	<b>Status:</b>	Final
<b>Security:</b>	Public	<b>Version:</b>	V1.0

---

The measurement of user-experienced data rate can be quite different in a high mobility scenario such as HST scenario where the mTEs deployed at the head and/or tail of a train communicates with mRUs deployed in a one-dimensional linear network, as seen in Figure 19.

In this situation, the mTE will experience variation in its data rate according to the distance-dependent path-loss and fading from the mRU. In addition, users in a train are supported via an onboard relay deployed inside the train carriage, so that they experience almost identical QoS similar to an indoor environment. From the above considerations, it is concluded that the number of users simultaneously achieving 100 Mbit/s user-experienced data rate can be inferred, for example, by calculating the 5th percentile data rate achieved at the mTE divided by the target data rate 100 Mbit/s.

Based on the aforementioned description on the user-experienced data rate and CDF results in Figure 24, we can estimate the number of simultaneously served users each achieving 100 Mbit/s user-experience in Table 4. It is important to note that these values are worst-case values (i.e., 5th percentile lowest value), much lower than the average values.

**Table 4 Number of simultaneously served users achieving 100 Mbit/s user-experience**

Transmission scheme	Speed		
	100 km/h	300 km/h	500 km/h
SFT	8.40 users	7.39 users	6.16 users
MFT	20.41 users	17.53 users	13.83 users



<b>Title:</b>	Deliverable D3.8: Final results on the mobility framework		
<b>Date:</b>	31 May 2018	<b>Status:</b>	Final
<b>Security:</b>	Public	<b>Version:</b>	V1.0

### 3 Analyzing the Positioning Data-Rate Trade-off in mm-Wave communications through Stochastic Geometry (CEA)

#### 3.1 Introduction

It is well known that mm-wave communication is characterized by high path loss and sensitivity to blockages. To solve these problems, beam-forming techniques are utilized with the help of highly directional antennas, which result in new issues in terms of coverage and initial access [18]. Moreover, beam-alignment errors between the BSs and the UEs degrade the communication performance.

One solution to this problem consists of enabling UEs to simultaneously receive signals in the mm-wave and in the sub-6GHz band, and to use the latter to support the initial access on the mm-wave band [19].

Another approach exploits positioning algorithms to support the UE cell discovery and access to mm-wave BSs. On the one hand, with fine-tuned positioning, the beam-alignment procedure is quickened, and beamforming and user tracking are improved [20]. On the other hand, improved mm-wave beam-forming can be used for more accurate localization and orientation of nodes [21].

Accordingly, we investigate whether the 5G CHAMPION vehicle-to-infrastructure architecture (see Figure 26 [22]) can be deployed for supporting positioning and broadband functionalities simultaneously, where the positioning function is mainly used to support the beam alignment between the mRU and the mTE. Specifically, we study the trade-off between positioning efficiency and downlink data rates and accordingly, we prescribe the operator an algorithm to tune the mRU transmit power so as to meet specific QoS requirements of different services.

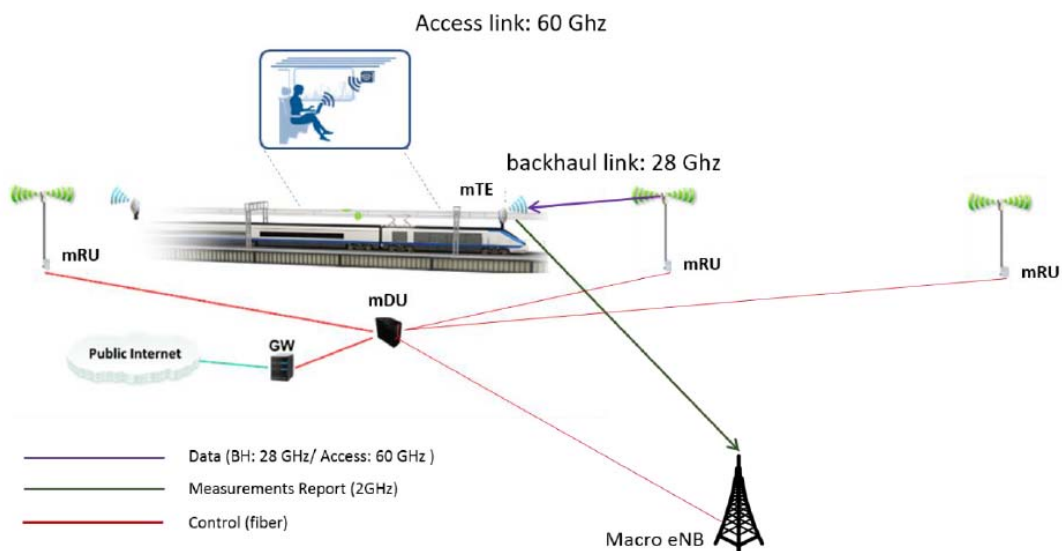


Figure 26: Proposed framework for HST communications [22].



---

<b>Title:</b>	Deliverable D3.8: Final results on the mobility framework		
<b>Date:</b>	31 May 2018	<b>Status:</b>	Final
<b>Security:</b>	Public	<b>Version:</b>	V1.0

---

### 3.1.1 Related Work

In the context of sub-6GHz systems, Jeong et al. [23] have studied a distributed antenna system providing both data communication and positioning functionalities. The authors assumed that the UEs know the positions of the BSs and attempt to estimate their own positions based on the received signals. Lemic et al. [24] have shown that localization using mm-wave frequencies is efficient in terms of accuracy, even in the presence of a limited number of anchor nodes. In fact, mm-wave beam-forming allows for accurate localization and orientation of UEs with respect to the BSs. Garcia et al. [20] have studied a location-aided initial access strategy for mm-wave networks, in which the information of UE locations enables to speed up the channel estimation and beam-forming procedures. Destino et al. [21] have studied the trade-off between communication rate and positioning quality in a single user mm-wave link. Similarly Koirala et al. [25] have studied the beamforming optimization and spectral power allocation based on theoretical localization bounds.

The downlink communication performance in random wireless networks is typically characterized by SINR coverage probability and rate coverage probability, using stochastic geometry [26]. For this, the positions of the BSs are modeled using homogeneous Poisson point process (PPP) [27] or using repulsive point processes [28]. Recently, Ghatak et.al. [29] investigated a more realistic scenario, where mm-wave BSs are deployed along the roads of a city. We use this model in this report, and accordingly we study a one dimensional setting where the BSs and the served users are assumed to be on the same street.

Specifically, leveraging on the tools of stochastic geometry, we present an average characterization of the localization and communication performance of this network, by exploiting the a-priori knowledge about the distribution of the distances of the users from the BSs. We analyze the positioning and data communication trade-off, and provide the operator with a power control scheme designed to satisfy distinct QoS requirements of the positioning and the communication functions.

## 3.2 System Model

### 3.2.1 Network Geometry

The positions of the mRUs are modeled as points of a one-dimensional PPP  $\phi$ , with intensity  $\lambda$  [ $\text{m}^{-1}$ ]. Each mRU is assumed to be equipped with directional antennas with beamwidth  $\theta$  and the difference of height between the mRU and mTE is assumed to be fixed and equal to  $\Delta h$ . Let the corresponding product of the directivity gains of the transmitting and receiving antennas be  $G_0$ . The transmit power of the mRUs is assumed to be  $P$ . Without loss of generality, we perform our analysis from the perspective of a typical mTE located at origin, which associates with the mRU that provides the highest downlink power.

Accordingly, the distribution of the distance  $d$  of the typical mTE from the serving mRU is given by [30]:

$$f_d(x) = 2\lambda \exp(-2\lambda x)$$

Furthermore, we assume that the network deployment is such that the performance of the mTE is noise-limited.

### 3.2.2 Path-loss

Due to the low local scattering, we consider a Nakagami fading for mm-wave communications [31] with parameter  $\eta_0$  and variance equal to 1. Furthermore, we assume a



---

<b>Title:</b>	Deliverable D3.8: Final results on the mobility framework		
<b>Date:</b>	31 May 2018	<b>Status:</b>	Final
<b>Security:</b>	Public	<b>Version:</b>	V1.0

---

path loss model where the power at the origin received from a mRU located at a distance  $d$  is given by  $P_r = K \cdot P \cdot g \cdot G_0 \cdot (d^2 + \Delta h^2)^{-\frac{\alpha}{2}}$ , where  $K$  is the path loss coefficient,  $g$  represents the fast-fading, and  $\alpha$  is the path loss exponent. Thus, the average SNR can be written as  $\frac{K \cdot P \cdot g \cdot G_0 \cdot (d^2 + \Delta h^2)^{-\frac{\alpha}{2}}}{N_0 \cdot B}$ , where  $N_0$  and  $B$  are the noise power density and the operating bandwidth, respectively.

### 3.2.3 Transmission Policy

We assume a communication scheme where the transmit power of the mRU is divided into two parts: one associated with positioning and the other allotted for data communication. The power allocated for localization determines the number of control symbols used for this function, whereas the remaining power is utilized for control and data symbols of the communication phase. We acknowledge that it is possible to utilize the native communication signal for positioning services. However, we use dedicated waveforms designed for better localization performance (e.g., see [32] for a discussion on localization specific waveforms). Hence, splitting of the transmit power becomes necessary to characterize and optimize the operating trade-off between communication and localization functionalities.

Accordingly, if the total transmit power is  $P$ , and  $\beta$  is the fraction of power used for data services, the corresponding transmit power for localization is  $P_L = (1 - \beta)P$ . Consequently, the transmit power for data service is  $P_D = \beta P$ . Let the SNR for the distance estimation and the data communications phases be represented by  $SNR_1$  and  $SNR_2$ , respectively.

## 3.3 Positioning Error, Data Rate Coverage, and Misalignment Error

In this section, we first characterize the minimum variance of the error in the estimation of the distance of the typical mTE from the serving mRU. Then, we derive the SNR coverage and the rate coverage probabilities.

### 3.3.1 Distance Estimation Analysis

To simplify our analysis, we only consider the effect of the distance on the power of the received signal (for instance, we consider RSSI based ranging algorithms), and ignore the effect of the distance on the phase [33]. Accordingly, the received signal is:

$$y(t) = \frac{\sqrt{KG_{0PL}}}{(d^2 + \Delta h^2)^{\frac{\alpha}{4}}} x(t) + n(t),$$

where  $x(t)$  is the transmitted signal and  $n(t)$  is a zero mean additive white Gaussian noise resulting in estimation errors.

#### Lemma 1:

The expected value of the Fisher information for the estimation of the distance  $d$  is calculated as:

$$J_D = \frac{KG_{0PL} 2\lambda \bar{f}^2}{N_0} \int_1^\infty \frac{\exp(-2\lambda x)}{(x^2 + \Delta h^2)^{\frac{\alpha}{2}}} dx,$$

where  $\bar{f}^2 = 1.25 \pi^2 B^2$ . Furthermore, the prior information is  $J_D = \log 2\lambda - 1$ .



<b>Title:</b>	Deliverable D3.8: Final results on the mobility framework		
<b>Date:</b>	31 May 2018	<b>Status:</b>	Final
<b>Security:</b>	Public	<b>Version:</b>	V1.0

Finally, the Bayesian information can be obtained as  $J_B = J_D + J_P$ . Consequently, the Bayesian Cramer-Rao Lower Bound (BCRLB) and Jeffrey's prior corresponding to the Bayesian information are calculated as  $\frac{1}{J_B}$  and  $\sqrt{J_B}$ , respectively.

### 3.3.2 Coverage and Rate Analysis

Based on the path-loss model of Section 3.2.2, the SNR for the communication phase is:

$$SNR_2 = \frac{P_D K \cdot g \cdot G_0 \cdot (d^2 + \Delta h^2)^{-\alpha}}{N_0 \cdot B}$$

Accordingly, let us define the SNR coverage probability of the typical mTE at a threshold  $\gamma$ , as the probability that the SNR is greater than  $\gamma$ . It represents the fraction of the users under coverage in the network.

#### Lemma 2:

The SNR coverage probability at a threshold of  $\gamma$  is calculated as [57]:

$$P_C(\gamma) = \sum_{n=1}^{n_0} (-1)^{n+1} \binom{n_0}{n} 2\lambda \exp\left(2\lambda - \frac{\Delta h^2 n \gamma N_0}{P_D K \cdot g \cdot G_0}\right) \left[ \frac{\sqrt{\pi}}{2} \left( \sqrt{\frac{P_D K \cdot g \cdot G_0}{n \gamma N_0}} - \frac{P_D K \cdot g \cdot G_0}{n \gamma N_0} \operatorname{erf}\left(\frac{\Delta h^2 n \gamma N_0}{P_D K \cdot g \cdot G_0}\right) \right) \right]$$

Similar to the SNR coverage probability, the rate coverage probability at a threshold  $r_0$  is defined as the probability that the downlink data rate of the typical user is greater than  $r_0$ .

#### Corollary 1:

The rate coverage probability can be computed as:

$$P_R(r_0) = P_C\left(2^{\frac{r_0}{B}} - 1\right).$$

### 3.3.3 Beam Misalignment Error

An mRU with an antenna beamwidth  $\theta$ , serving an mTE located at distance  $d$ , covers a region of length  $D_0$  on the ground (see Figure 27). Using simple trigonometric calculations, we have:

$$D_0 = \frac{2 \tan\left(\frac{\theta}{2}\right) \left(1 + \frac{d^2}{\Delta h^2}\right)}{1 - \frac{d^2}{\Delta h^2} \tan^2\left(\frac{\theta}{2}\right)}$$

Once the localization procedure and the corresponding exchange of mTE-mRU control signals is performed, beam-misalignment can occur in the absence of dynamic beam-alignment on both sides of the radio link. Assuming that the mTE's antenna is always oriented towards the mRU, beam-misalignment will occur in case the distance of the mTE is more than  $\frac{D_0}{2}$  from the estimated one.



<b>Title:</b>	Deliverable D3.8: Final results on the mobility framework		
<b>Date:</b>	31 May 2018	<b>Status:</b>	Final
<b>Security:</b>	Public	<b>Version:</b>	V1.0

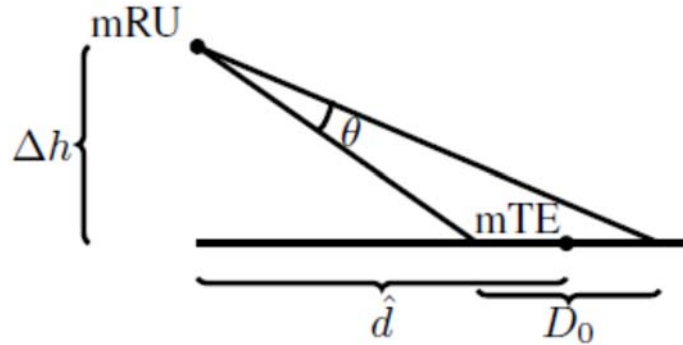


Figure 27: Coverage region for a beamwidth  $\theta$ .

Let us assume that the estimation error for the mTE localization is symmetric about its mean. Consequently, we bound the probability of the beam-misalignment as follows:

**Lemma 3:**

The probability of beam-misalignment for an mTE located at a distance  $d$  from the serving mRU is bounded as

$$P_{MA}(d) \leq \frac{2BCRLB}{D_0}.$$

In the next section, we prescribe guidelines for an operator to choose an operating beamwidth  $\theta$  for limiting this error.

### 3.4 Numerical Results and Discussion

In this section, we present some numerical results based on the analytical framework presented in the previous sections. First, we show how the SNR coverage probability changes with the power splitting factor  $\beta$ . Subsequently, we study the trade-off between localization and data rate as a function of  $\beta$ . Then, with the help of two examples, we describe our power partitioning scheme. In the following analysis, we assume  $G_0 = 10$  dB and  $n_0 = 3$ .

#### 3.4.1 SINR Coverage Probability

In Figure 28 we plot the SNR coverage probability with respect to  $\beta$  at a threshold of  $\gamma = -10$  dB. As  $\beta$  increases, the SINR coverage probability increases due to more power allocated to the data transmission phase. This provides a guideline to select a minimum operating  $\beta$  for a given deployment density, such that the outage is limited. As an example, to limit a service outage below 20%, with an mRU deployment of  $1 \text{ km}^{-1}$  and a power budget of  $P = 25$  dBm, the minimum  $\beta$  is 0.15, whereas with a power budget of  $=20$  dBm, the minimum  $\beta$  is 0.5.

More interestingly, this analysis provides the operator dimensioning rules in terms of the deployment density of the mRUs for a given power budget. For example, in order to support services with an outage tolerance of 10%, with a power budget of 20 dBm, a deployment density of  $1 \text{ km}^{-1}$  does not suffice, and the operator must necessarily deploy more mRUs.

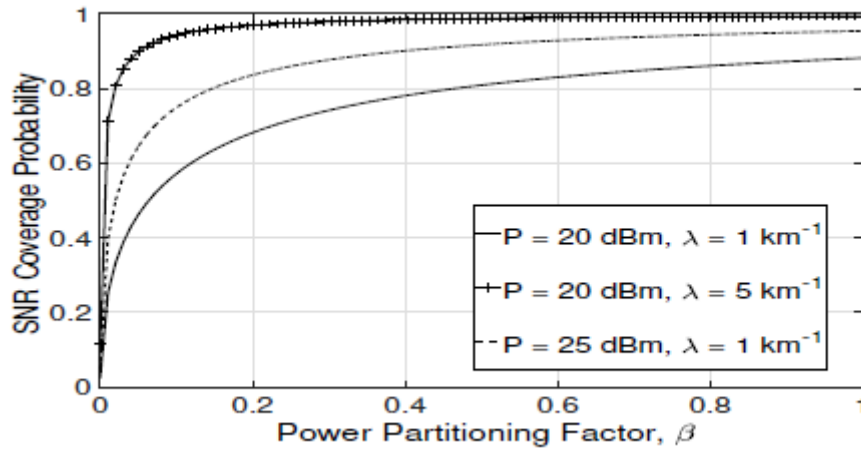


Figure 28: SNR coverage probabilities for a threshold of  $\gamma = -10$  dB vs the fractional power split for different  $\lambda$ .

### 3.4.2 Misalignment Error

In Figure 29 we plot the mean beam-misalignment bound with respect to the beamwidth of the transmit antenna of the mRUs. As expected, a larger beamwidth and higher SNR lower the misalignment. For example, for a tolerable misalignment of 0.02% with SNR = -15 dB and  $\lambda = 5$  km $^{-1}$  the minimum antenna beamwidth should be 8 degrees.

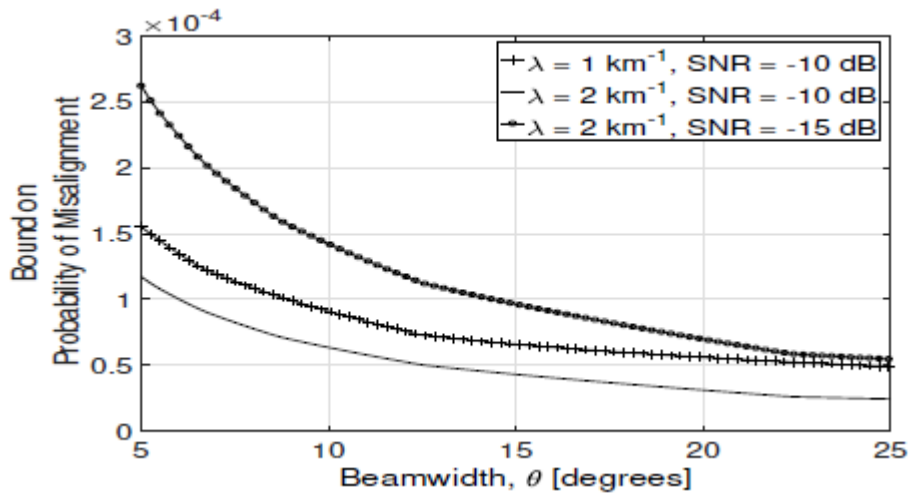


Figure 29: Beam misalignment error with respect to beamwidth of the transmit antenna.



<b>Title:</b>	Deliverable D3.8: Final results on the mobility framework		
<b>Date:</b>	31 May 2018	<b>Status:</b>	Final
<b>Security:</b>	Public	<b>Version:</b>	V1.0

### 3.4.3 Distance Estimation-Data Rate Trade-off

In Figure 30 we plot the trade-off between the efficiency of the distance estimation of the user, represented by its Jeffrey's prior<sup>1</sup> and the rate coverage probability at a rate threshold  $r_0=500$  Mbps. Each position in the plot for a given deployment parameter corresponds to a particular  $\beta$ . Thus for a given power budget, deployment density, and operating beamwidth, the performance of the system is determined by a particular operating characteristic, i.e., a trade-off between the positioning efficiency and data rate performance. For a particular operating characteristic, as we increase  $\beta$ , we improve the rate coverage probability at the cost of degrading the localization efficiency; whereas, decreasing  $\beta$  has the opposite effect. Accordingly, there exists a trade-off between the distance estimation and the data rate performance of the system. In the next subsection, we propose a scheme for selecting  $\beta$  based on a given operating beamwidth.

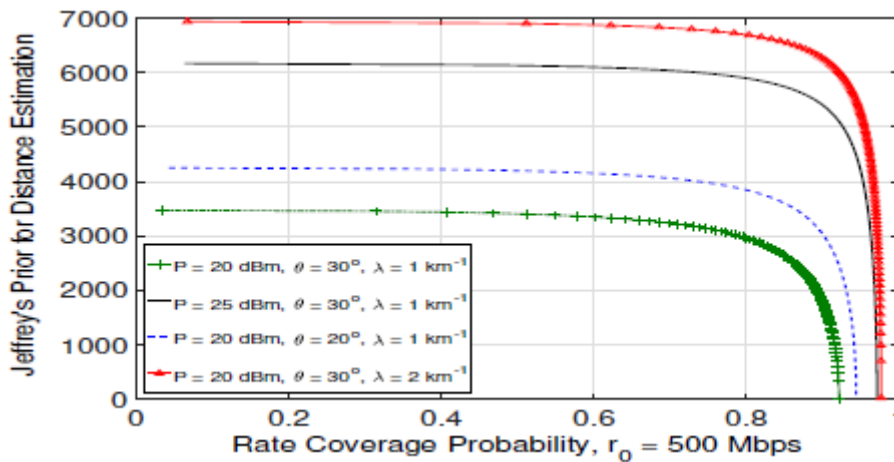


Figure 30: Distance estimation error vs physical data rate for different power budget.

### 3.4.4 QoS Aware Network Parameter Setting

We propose the following scheme for setting the network parameters. First, for a given power budget, a deployment density, and an operating beamwidth, the corresponding operating characteristic (i.e., a trade-off curve from Figure 30) is selected. Next, for the chosen operating characteristic, the minimum  $\beta_{min}$  is chosen to satisfy the required outage constraint. Then, for a given positioning error constraint, the maximum value of  $\beta$ , i.e.,  $\beta_{max}$  is selected. Finally, the operating  $\beta_{min} \leq \beta \leq \beta_{max}$  is selected to address the specific QoS requirements.

Accordingly, the misalignment error varies for the chosen  $\beta$  and the operating  $\theta$ . In what follows, we explain the total power distribution based on the QoS requirements, for a varying degree of misalignment. We assume a network with  $\lambda = 2 \text{ km}^{-1}$  and an mRU power budget of  $P = 20 \text{ dBm}$  providing two services:

- Service 1 requires maximum positioning efficiency and a tolerable outage of 10%.
- Service 2 requires maximum data-rate and a tolerable positioning error of  $5e-4 \text{ m}$ .

<sup>1</sup> The estimation error is calculated as the inverse of the Jeffrey's prior.



<b>Title:</b>	Deliverable D3.8: Final results on the mobility framework		
<b>Date:</b>	31 May 2018	<b>Status:</b>	Final
<b>Security:</b>	Public	<b>Version:</b>	V1.0

We study the power partitioning scheme under different operating beamwidths. In practice, the operating beamwidth may be a system requirement for the first generation mmWave networks. Intuitively, for a less stringent misalignment requirement, the operating beamwidth can be smaller. This can either be exploited to improve the positioning or enhance the data-rate, as per the required QoS.

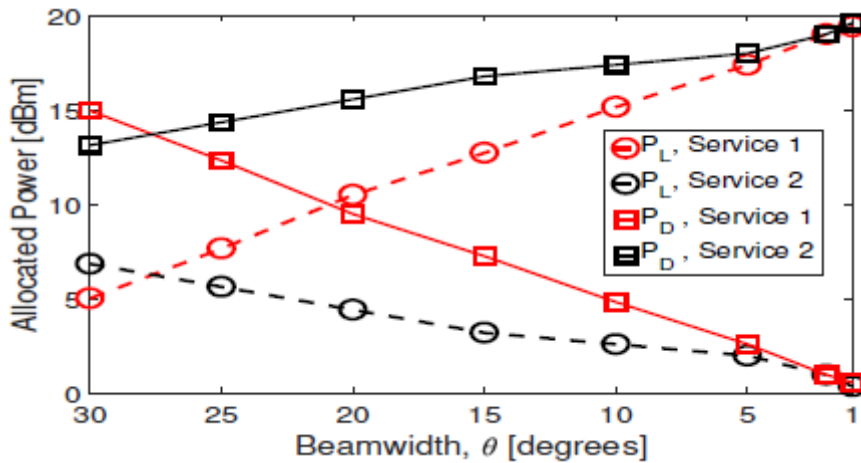


Figure 31: Distance estimation error vs physical data rate for different power budget.

For service 1, the operator should set  $\beta$  equal to the  $\beta_{min}$  corresponding to the  $\theta$  that satisfies the misalignment requirement. Then, if the operating  $\theta$  can be decreased, more power can be allotted for positioning and the one used for data communication  $P \cdot \beta_{min}$  is reduced, accordingly. On the other hand, the operator should set  $\beta$  equal to the  $\beta_{max}$  corresponding to the  $\theta$  that satisfies the misalignment requirement. Therefore, a thinner beamwidth facilitates larger power allocation for data communication ( $P_D$  increases).

The stark difference in the two examples lies in the fact that the advantage of operating with a thinner beamwidth is exploited differently. With decreasing  $\theta$ , for a positioning service,  $P_L$  increases and  $P_D$  decreases, whereas the opposite is true for the high data-rate services. It is worth to mention that the inter-dependence of  $\beta$  and  $\theta$  for controlling the positioning performance and the misalignment error is not trivial. As an example, for a required misalignment constraint or for a required positioning error constraint, there exist non-unique  $(\theta, \beta)$  pairs. For reducing the misalignment, either  $\theta$  should be increased, or  $\beta$  should be decreased. However, increasing  $\theta$  has an adverse effect on the BCRLB that can be circumvented by further decreasing  $\beta$ . This calls for suitable algorithms to obtain an optimal  $(\theta, \beta)$  pair. Furthermore, it may happen that for a given  $\theta$  and  $P$ , no feasible  $\beta$  exists that satisfies the positioning and misalignment constraints simultaneously, thereby necessitating a higher mRU power budget.

### 3.4.5 Conclusion

In this study, we investigate whether the 5G CHAMPION vehicle-to-infrastructure architecture can be deployed to support positioning and broadband services simultaneously. Specifically, we introduced a power-partitioning based mechanism that enables the mm-wave mRU to satisfy different localization and data-rate requirements. In this context, we derived dimensioning rules in terms of the density of mRUs required to limit outage probability. Then we provided the operator with a beamwidth selection guideline to limit the misalignment



<b>Title:</b>	Deliverable D3.8: Final results on the mobility framework		
<b>Date:</b>	31 May 2018	<b>Status:</b>	Final
<b>Security:</b>	Public	<b>Version:</b>	V1.0

probability. Finally, we studied the trade-off between the localization efficiency and the downlink data rate, and consequently, presented a scheme for partitioning the transmit power depending on the service requirements.

## 4 Mobility management techniques and architecture

### 4.1 Coverage analysis and performance evaluation of HST under linear deployment architecture (ETRI)

#### 4.1.1 Scenario description

The HST scenario intends to provide broadband Internet access to passengers inside of a train carriage. In order to provide continuous coverage along the track, linear deployment of RRHs is assumed, as seen in Figure 32. Beamforming technique can be employed both at the RRHs and at the train to form a narrow and high-gain beam along the track, thereby providing linear coverage. Since the additional gain of beam steering is not significant in this scenario, we assume a fixed and uni-directional beamforming. Thanks to the mmWave (e.g., around 30 GHz) having very short wavelength, large array can be implemented with a relatively small antenna form factor.

The UEs inside the train are assumed to communicate with access points (APs) installed in each train carriage. The APs are connected to the onboard relay deployed at the head of the train and relay user data streams between the RRHs and UEs. The link between the AP and UEs can be established via WiFi or femto cells. Inside the train carriage, the radio characteristics are similar to those of an indoor environment, and the transmission is done independently of the link between the RRH and the onboard relay. Hence, we focus on the link between the RRH and onboard relay rather than the link between the AP and UEs.

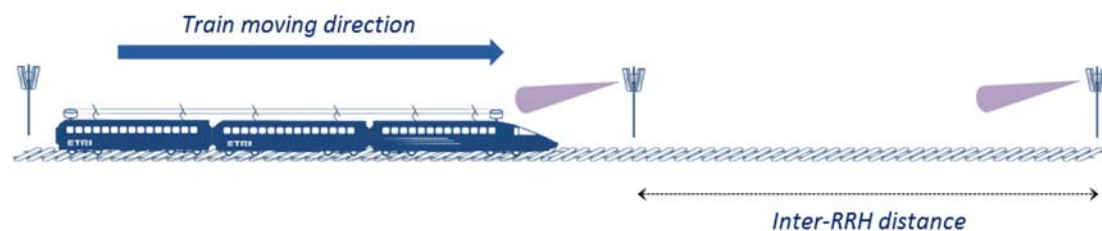


Figure 32 Linear deployment architecture for HST

#### 4.1.2 Coverage analysis under Nakagami-m fading channel assumption

Simple and accurate mathematical modeling of the mmWave channel is a prerequisite for conducting performance analysis. According to extensive mmWave channel measurement campaigns [34], [35], mmWave signals experience large path-losses due to Friis' transmission law, atmospheric absorption, and rain attenuation. In addition, mmWave signals are much more sensitive to the existence of LoS than the microwave signals [36]. In a LoS dominant scenario, we expect quasi-optical propagation due to the limited reflection and scattering, yielding AWGN-like channels [37]. Oppositely, in an NLoS dominant scenario, mmWave signals experience Rayleigh-like small-scale fading [38], [39]. Hence, in order to fully reflect the characteristics of mmWave propagation, a more general fading channel model is needed. One candidate for such a general fading channel is the Nakagami-m fading



<b>Title:</b>	Deliverable D3.8: Final results on the mobility framework		
<b>Date:</b>	31 May 2018	<b>Status:</b>	Final
<b>Security:</b>	Public	<b>Version:</b>	V1.0

channel, where a power ratio between the LoS and NLoS components can be determined by the  $m$  parameter.

For the path-loss modeling, a standard path loss model is used with a path loss exponent  $\alpha > 2$ , and we assume the channel gains between the BSs and the mobile users experience Nakagami- $m$  fading. The Nakagami- $m$  fading channel model well characterizes a realistic multi-path channel where both the LoS and the NLoS components exist with two special cases: Rayleigh fading ( $m = 1$ ) and AWGN ( $m \rightarrow \infty$ ). The corresponding channel power gains will be Gamma distributed with the probability density function (PDF) of  $f_x(x) = \frac{m^m}{\Gamma(m)} x^{m-1} e^{-mx}$  [25]. We denote the channel power gain of a desired mobile user as  $h$ .

All the RRHs are assumed to have a constant transmit power  $P$  [40], [41]. We also assume that there is no interference from other RRHs, considering the large distance between consecutive trains in HST environment. The inter-RRH distance is constant  $R$ . Then, the resulting signal-to-noise ratio (SNR) at the train receiver is given by

$$\text{SNR} = \frac{hr^{-\alpha}P}{N_0}$$

where  $r$  is the distance between the RRH and the transceiver at the train and  $N_0$  is the noise power, respectively.

Here, we analyze coverage probability, which is defined as the probability that a typical mobile terminal is in coverage. In other words, we consider a specific terminal is in coverage if its received SNR exceeds a target threshold  $T$ :

$$P_c \triangleq \Pr[\text{SNR} > T]$$

Since the distance  $r$  and the channel power gain  $h$  are both random variables, the above coverage probability can be expressed as

$$P_c = \int_0^R \Pr\left[h > \frac{r^\alpha N_0 T}{P}\right] dr$$

Substituting the complementary cumulative distribution function (CCDF) of the Gamma distribution  $F_x^c(x) = \frac{\Gamma(m, mx)}{\Gamma(m)} = e^{-mx} \sum_{k=0}^{m-1} \frac{(mx)^k}{k!}$ , we have

$$P_c = \frac{1}{R} \sum_{k=0}^{m-1} \frac{1}{k!} \left(\frac{mN_0 T}{P}\right)^k \int_0^R r^{k\alpha} e^{-\frac{mN_0 T}{P} r^\alpha} dr$$

Integrating using (3.381.8) of [42] yields the desired closed-form expression for the coverage probability:

$$P_c = \frac{1}{R\alpha} \sum_{k=0}^{m-1} \frac{1}{k!} \left(\frac{mN_0 T}{P}\right)^{1/\alpha} \gamma\left(\frac{k\alpha + 1}{\alpha}, \frac{mN_0 T R^\alpha}{P}\right)$$

where  $\gamma(a|x) = \int_0^x e^{-t} t^{a-1} dt$  is the incomplete Gamma function.

We plotted coverage probability as a function of SNR for different  $m$  values in Figure 33. We can see that the coverage probability increases as  $m$  increases, which means that stronger fading degrades the coverage probability due to the increased channel randomness.



**Title:** Deliverable D3.8: Final results on the mobility framework  
**Date:** 31 May 2018 **Status:** Final  
**Security:** Public **Version:** V1.0

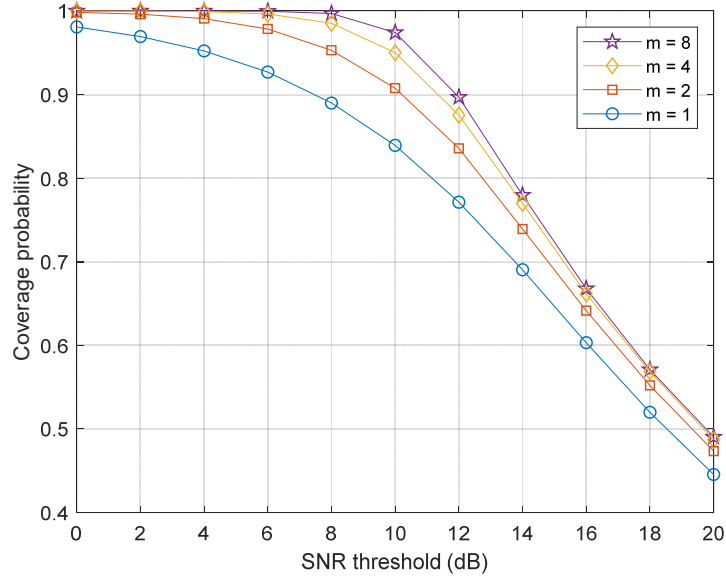


Figure 33 Coverage probability vs. SNR for different  $m$  values

#### 4.1.3 Performance evaluation under 3GPP HST channel environment

We further conducted performance evaluation of the HST based on the 3GPP 5G NR channel model. The following assumptions were made:

##### Antenna configuration:

A uniform rectangular panel array antenna is assumed for both the RRH and the relay onboard the train. The antenna elements are uniformly placed on the two-dimensional antenna panel. We employ an 8x8 antenna configuration at both the RRH and the onboard relay. The antenna element spacings are assumed to be  $0.5\lambda$ . The radiation pattern for each antenna element is defined in [43], reproduced below:

$$A''(\theta'', \phi'') = -\min\{-[A_{E,V}(\theta'') + A_{E,H}(\phi'')], A_m\}$$

where

$$A_{E,V}(\theta'') = -\min\left\{12 \left(\frac{\theta'' - 90^\circ}{\theta_{3dB}}\right)^2, SLA_V\right\}$$

$$A_{E,H}(\phi'') = -\min\left\{12 \left(\frac{\phi''}{\phi_{3dB}}\right)^2, A_m\right\}$$

with  $\theta_{3dB} = \phi_{3dB} = 65^\circ$  and  $SLA_V = A_m = 30$  dB.

##### Channel model for link-level simulation:

For the link-level simulation, the clustered delay line (CDL) model is used. Among the five CDL models, the CDL-D model is agreed for the 3GPP 5G NR HST scenario [44], where the Rician K-factor is 13.3 dB and the scaling of delay spread is 10ns. The power delay profile of the selected CDL-D model is given in Table 5. It is clear that the LoS path dominates the



<b>Title:</b>	Deliverable D3.8: Final results on the mobility framework		
<b>Date:</b>	31 May 2018	<b>Status:</b>	Final
<b>Security:</b>	Public	<b>Version:</b>	V1.0

channel power. Intra-cluster angular spread values for the HST scenario are given as  $c_{ASD} = c_{ASA} = 5^\circ$  and  $c_{ZSD} = c_{ZSA} = 1^\circ$  [45].

**Table 5 Power delay profile of CDL-D channel model with scaling of delay spread of 10ns**

Cluster (#)	Delay (ns)	Power (dB)	AoD ( $^\circ$ )	AoA ( $^\circ$ )	ZoD ( $^\circ$ )	ZoA ( $^\circ$ )
1 (LoS)	0	-0.2	0	-180	98.5	81.5
1 (NLoS)	0	-13.5	0	-180	98.5	81.5
2	0.35	-18.8	89.2	89.2	85.5	86.9
3	6.12	-21	89.2	89.2	85.5	86.9
4	13.63	-22.8	89.2	89.2	85.5	86.9
5	14.05	-17.9	13	163	97.5	79.4
6	18.04	-20.1	13	163	97.5	79.4
7	25.96	-21.9	13	163	97.5	79.4
8	17.75	-22.9	34.6	-137	98.5	78.2
9	40.42	-27.8	-64.5	74.5	88.4	73.6
10	79.37	-23.6	-32.9	127.7	91.3	78.3
11	94.24	-24.8	52.6	-119.6	103.8	87
12	97.08	-30	-132.1	-9.1	80.3	70.6
13	125.25	-27.7	77.2	-83.8	86.5	72.9

### **Channel coefficient generation:**

The channel coefficient generation of the CDL model consists the following steps [43]:

- Step 1: Departure and arrival angles generation according to the per-cluster departure and arrival angles and the ray offset angles within a cluster.
- Step 2: Coupling of departure and arrival rays within a cluster.
- Step 3: Cross-polarization power ratios generation for each ray.
- Step 4: Channel coefficient generation.

The channel coefficient  $H_{u,s}(\tau, t)$  between receive antenna  $u$  and transmit antenna  $s$  at time instance  $t$  and delay  $\tau$  is defined as

$$H_{u,s}(\tau, t) = \sqrt{\frac{1}{K+1}} \sum_{n=1}^N H_{u,s,n}^{\text{NLoS}}(t) \delta(\tau - \tau_n) + \sqrt{\frac{K}{K+1}} H_{u,s,1}^{\text{LoS}}(t) \delta(\tau - \tau_1)$$

where  $K$  is the Rician  $K$ -factor in a linear scale and  $\tau_n$  is the delay of the  $n$ -th cluster.  $\delta(\cdot)$  is Dirac's delta function.

For each NLoS cluster,  $H_{u,s,n}^{\text{NLoS}}(t)$

$$H_{u,s,n}^{\text{NLoS}}(t) = \sqrt{\frac{P_n}{M}} \sum_{m=1}^M \begin{bmatrix} F_{rx,u,\theta}(\theta_{n,m,ZOA}, \phi_{n,m,AOA}) \\ F_{rx,u,\phi}(\theta_{n,m,ZOA}, \phi_{n,m,AOA}) \end{bmatrix}^T \begin{bmatrix} \exp(j\Phi_{n,m}^{\theta\theta}) & \sqrt{\kappa_{n,m}^{-1}} \exp(j\Phi_{n,m}^{\theta\phi}) \\ \sqrt{\kappa_{n,m}^{-1}} \exp(j\Phi_{n,m}^{\phi\theta}) & \exp(j\Phi_{n,m}^{\phi\phi}) \end{bmatrix} \\ \times \begin{bmatrix} F_{tx,s,\theta}(\theta_{n,m,ZOD}, \phi_{n,m,AOD}) \\ F_{tx,s,\phi}(\theta_{n,m,ZOD}, \phi_{n,m,AOD}) \end{bmatrix} \exp\left(j2\pi \frac{\hat{r}_{rx,n,m}^T \cdot \bar{d}_{rx,u}}{\lambda_0}\right) \exp\left(j2\pi \frac{\hat{r}_{tx,n,m}^T \cdot \bar{d}_{tx,u}}{\lambda_0}\right) \exp\left(j2\pi \frac{\hat{r}_{rx,n,m}^T \cdot \bar{v}}{\lambda_0} t\right)$$

The information contained in this document is the property of the contractors. It cannot be reproduced or transmitted to thirds without the authorization of the contractors.



<b>Title:</b>	Deliverable D3.8: Final results on the mobility framework		
<b>Date:</b>	31 May 2018	<b>Status:</b>	Final
<b>Security:</b>	Public	<b>Version:</b>	V1.0

where

- $P_n$ : the power of the  $n$ -th cluster in a linear scale
- $F_{rx,u,\theta}(\cdot, \cdot)$ ,  $F_{rx,u,\phi}(\cdot, \cdot)$ : the receive antenna radiation patterns in the direction of  $\theta$  and  $\phi$ , respectively
- $F_{tx,s,\theta}(\cdot, \cdot)$ ,  $F_{tx,s,\phi}(\cdot, \cdot)$ : the transmit antenna radiation patterns in the direction of  $\theta$  and  $\phi$ , respectively
- $\{\Phi_{n,m}^{\theta\theta}, \Phi_{n,m}^{\theta\phi}, \Phi_{n,m}^{\phi\theta}, \Phi_{n,m}^{\phi\phi}\}$ : set of random initial phases for four different polarization combinations, i.e.,  $\theta\theta$ ,  $\theta\phi$ ,  $\phi\theta$ , and  $\phi\phi$
- $\kappa_{n,m}$ : the cross polarization power ratio (XPR) for  $n$ -th cluster and  $m$ -th ray
- $\lambda_0$ : wavelength of the carrier frequency
- $\hat{r}_{rx,n,m}^T$ ,  $\hat{r}_{tx,n,m}^T$ : spherical unit vectors of receive and transmit antennas, respectively
- $\bar{d}_{rx,u}$ ,  $\bar{d}_{tx,u}$ : location vectors of receive and transmit antennas, respectively
- $\bar{v}$ : velocity vector

For the LoS path,  $H_{u,s,1}^{LoS}(t)$  is given by

$$H_{u,s,1}^{LoS}(t) = \begin{bmatrix} F_{rx,u,\theta}(\theta_{LOS,ZOA}, \phi_{LOS,AOA}) \\ F_{rx,u,\phi}(\theta_{LOS,ZOA}, \phi_{LOS,AOA}) \end{bmatrix}^T \begin{bmatrix} \exp(j\Phi_{LOS}) & 0 \\ 0 & -\exp(j\Phi_{LOS}) \end{bmatrix} \\ \times \begin{bmatrix} F_{tx,s,\theta}(\theta_{LOS,ZOD}, \phi_{LOS,AOD}) \\ F_{tx,s,\phi}(\theta_{LOS,ZOD}, \phi_{LOS,AOD}) \end{bmatrix} \exp\left(j2\pi \frac{\hat{r}_{rx,LOS}^T \cdot \bar{d}_{rx,u}}{\lambda_0}\right) \exp\left(j2\pi \frac{\hat{r}_{tx,LOS}^T \cdot \bar{d}_{tx,u}}{\lambda_0}\right) \exp\left(j2\pi \frac{\hat{r}_{rx,LOS}^T \cdot \bar{v}}{\lambda_0} t\right)$$

### **Simulation results:**

We provide link-level simulation results for the HST scenario based on the aforementioned channel model. The detailed simulation parameters are summarized in Table 6

**Table 6 Link-level simulation parameters**

Parameter	Value
Carrier frequency	30 GHz
System bandwidth	80 MHz
Subcarrier spacing	120 kHz
Channel coding	LTE Turbo
Number of layers	1
Channel estimation	Realistic
Equalizer	LMMSE
Channel model	<ul style="list-style-type: none"> <li>• CDL-D (DS = 10ns, K-factor = 7 dB)</li> <li>• Parameter set # 1: 5(ASD), 15(ASA), 5(ZSA), 1(ZSD) ZoD and ZoA for cluster #1 are fixed at 90 degrees</li> </ul>
TRP antenna configuration	(M,N,P,Mg,Ng) = (8,8,2,1,1); (dV,dH) = (0.5, 0.5) $\lambda$ with directional antenna element (HPBW=65°, directivity 8dB)
UE antenna configuration	(M,N,P,Mg,Ng) = (8,8,2,1,1); (dV,dH) = (0.5, 0.5) $\lambda$ with directional antenna element (HPBW=65°, directivity 8dB)



**Title:** Deliverable D3.8: Final results on the mobility framework  
**Date:** 31 May 2018      **Status:** Final  
**Security:** Public      **Version:** V1.0

Phase noise model	Multi-pole/zero model [46]
-------------------	----------------------------

Spectral efficiency is plotted as a function of SNR in Figure 34. The modulation coding scheme (MCS) is adjusted such that the block error rate (BLER) of 10% is satisfied. It shows that although performance degradation is observed for the 500 km/h case compared to the 350 km/h case, more than 1 bps/Hz is achieved for 500 km/h when the SNR is larger than 10 dB, which is much larger than with traditional LTE.

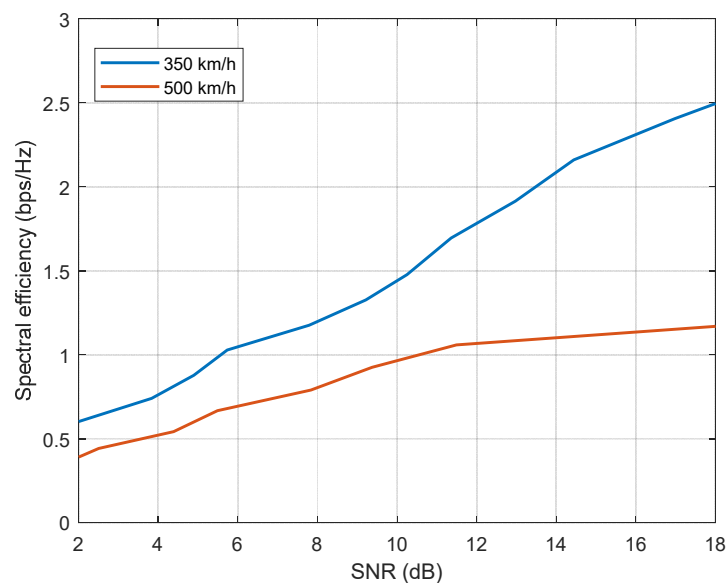


Figure 34 Spectral efficiency vs. SNR for 3GPP HST channel environment

## 4.2 Random access performance evaluation and handover triggering for HST (ETRI)

### 4.2.1 3GPP 5G NR preamble formats for mmWave based HST communications

For fulfilling the requirements of 5G wireless communication systems released by the ITU-R in September of 2015, the 3GPP decided to develop a NR access technology in 2016 and started to draft the 1<sup>st</sup> release of NR technical specifications in 2017 [47][48].

The main features of 3GPP 5G NR systems can be concluded as

- 1) enabling mm-Wave frequency bands;
- 2) enabling multiple numerologies; and
- 3) enabling multi-beam operation through hybrid beamforming.

Correspondingly, the latest NR PRACH design with the above mentioned features is introduced in this section [49][50][51].



<b>Title:</b>	Deliverable D3.8: Final results on the mobility framework		
<b>Date:</b>	31 May 2018	<b>Status:</b>	Final
<b>Security:</b>	Public	<b>Version:</b>	V1.0

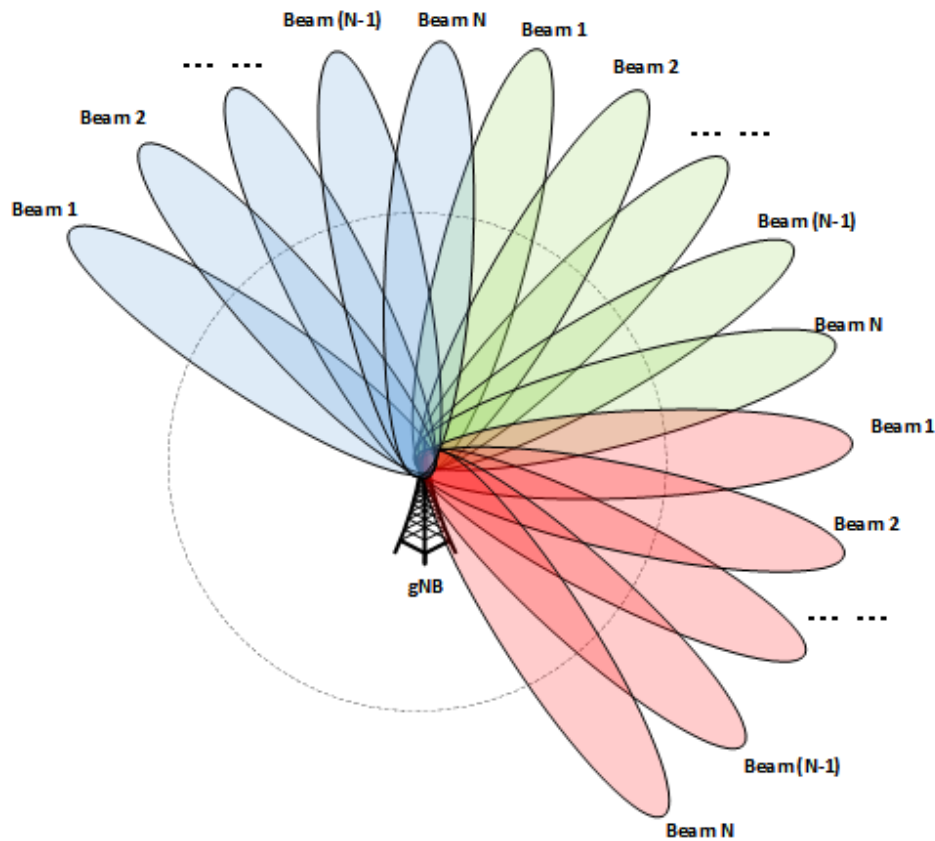


**Figure 35. Example of multiple beams at gNB**

In order to meet 5G requirements, mmWave frequency band up to 70 GHz is adopted in NR system for enhancement of system throughput. Furthermore, massive MIMO enabling multi-beam operations are adopted. In order to overcome the severe signal power degradation in mmWave bands due to propagation losses, the beams both at BS and UE sides must be very sharp for obtaining higher beamforming gain. Figure 35 shows an example of multiple beams at NR BS (which is also known as gNodeB or gNB).

In NR, preamble formats with a long sequence length of 839 complex symbols and a short sequence length of 139 complex symbols are defined [49][50][51]. There are four long sequence preamble formats indexing from 0 to 3. The long sequence formats can be only used in sub-6 GHz systems. Since NR supports multiple numerologies, the SCS in formats 0, 1 and 2 is 1.25 kHz when the SCS of format 3 is 5 kHz. A wider SCS of 5 kHz in format 3 is designed to compensate for higher Doppler spreads in high speed scenarios. Similar as in LTE-Pro systems, two restricted sets of preamble root indices are employed in NR corresponding to different UE mobility in case of long preamble formats. On the other hand, restricted sets are not supported for short sequence preamble formats since the SCS of short sequence preamble formats is within the scope of {15 kHz, 30 kHz, 60 kHz, 120 kHz}, which



**Title:** Deliverable D3.8: Final results on the mobility framework  
**Date:** 31 May 2018 **Status:** Final  
**Security:** Public **Version:** V1.0

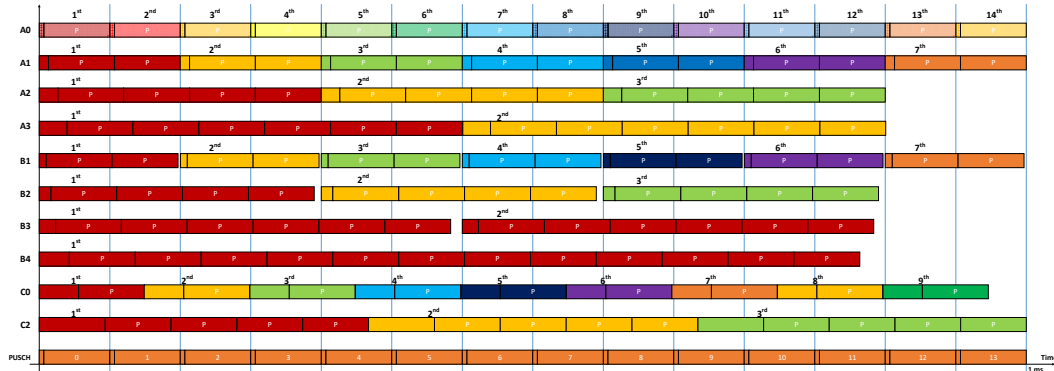


Figure 36. Comparison of NR short preamble formats with reference PUSCH SCS of 15kHz

are large enough to compensate for the Doppler spread of 500 km/h mobility. Note that the short sequence preamble formats can be used for both sub-6 GHz systems and above 6 GHz systems. When short sequence preamble formats are used for sub-6 GHz system, the SCS is either 15 kHz or 30 kHz, and when they are used for above 6 GHz systems, the SCS is either 60 kHz or 120 kHz. Similar as LTE systems, parameters such as SCS, preamble formats, physical resource allocation of PRACH channel and PRACH periodicity, are configured to an IDLE mode UE through the PRACH configuration table and RMSI. On-demand system information and RRC signaling can be used for delivering PRACH related parameters to CONNECTED mode UEs.

Since only short preamble formats are applicable for mmWave bands, and the designed HST communication within the scope of this project employs mmWave carrier frequencies only, we focus on the implementation and evaluation of the NR short sequence preamble formats only in this deliverable. Figure 36 shows the comparison among various NR short preamble formats when 15 kHz PUSCH SCS is used for reference. As shown in Figure 36, the short sequence preamble formats have three categories:

- 1) A and C types formats have a CP but no GT;
- 2) B type formats contain both CP and GT for each preamble.

In most of the short preamble formats, more than one preamble sequence is included. These multiple sequences within a preamble formats can be used for UL Rx beam calibration via beam sweeping operation. For example, format B3 can be used to find one optimal UL Rx beam out of six beams at gNB though Rx beam sweeping. Note that not all of the short sequence preamble formats are applicable for all of the message 1 numerologies, which depends on the power on-off time mask for each preamble format with different numerologies. For example after evaluation by the RAN WG4 of 3GPP, format A0 shows problem with SCS of 30 kHz, 60 kHz, and 120 kHz. So A0 will not be supported in NR release 15 specification. In order to successfully connect to the gNB, the optimal DL beam index at the gNB Tx side needs to be reported by the UE through message 1 transmission in NR. This can be done by the physical resource mapping for different UEs. In priori to PRACH transmission, the gNB should first map all of its Tx beams to different PRACH resources and let the UE know the downlink Tx beam to PRACH resource mapping though configuration. This mapping is achieved by association between the SSB and PRACH resources. With this information at



---

<b>Title:</b>	Deliverable D3.8: Final results on the mobility framework		
<b>Date:</b>	31 May 2018	<b>Status:</b>	Final
<b>Security:</b>	Public	<b>Version:</b>	V1.0

---

the UE, the gNB can know the optimal DL Tx beam to a specific UE after finding out the PRACH resources used by this UE for its message 1 transmission.

## 4.2.2 Simulation evaluation of short length preamble formats in HS scenario

### 4.2.2.1 Simulation parameters

*Table 7 Simulation parameters*

Carrier Frequency	30 GHz
Channel Model	TDL-D, AWGN with delay scaling values of 30 ns
Preamble format	A0
Preamble subcarrier spacing	60 kHz, 120 kHz
Antenna Configuration at BS	(4,8,2), with directional antenna element (HPBW=65°, directivity 8dB)
Antenna Configuration at UE/MR	(2,4,2), with directional antenna element (HPBW=90°, directivity 5dB)
Frequency Offset	+/- 0.05 ppm at TRP, +/-0.1 ppm at UE

Since only short length preamble formats can be applied in above-6GHz case, we evaluate the performance of short length preamble format in HST communications in this section. The simulation parameters are summarized in Table 7. Note that these simulation parameters are a simplified version of parameters for link level evaluating the performance of RACH preambles from a contribution [52] discussed during 3GPP RAN1 meeting #86.

During the simulations, the shortest preamble format A0 is selected for reducing the preamble length as well as the simulation time. TDL-D models defined in [53] are adopted where a LoS component exists.

### 4.2.2.2 Simulation results

According to the parameter table above, we can simply calculate that the maximum Doppler shift is 13.9 kHz when the HST mobility is 500 km/h. This value is relatively small compared to the preamble subcarrier spacings of 60 kHz or 120 kHz. When taking the frequency offset due to oscillators at TRP and UE side into account, the accumulated frequency offset is within the range of [-18.3 kHz, 18.3kHz]. We observed that this accumulated theoretical maximum frequency offset is less than 24 kHz, which value is 40% of 60 kHz subcarrier spacing. Therefore, the restricted sets of roots for generating short preamble formats are not necessary in NR systems.



<b>Title:</b>	Deliverable D3.8: Final results on the mobility framework		
<b>Date:</b>	31 May 2018	<b>Status:</b>	Final
<b>Security:</b>	Public	<b>Version:</b>	V1.0

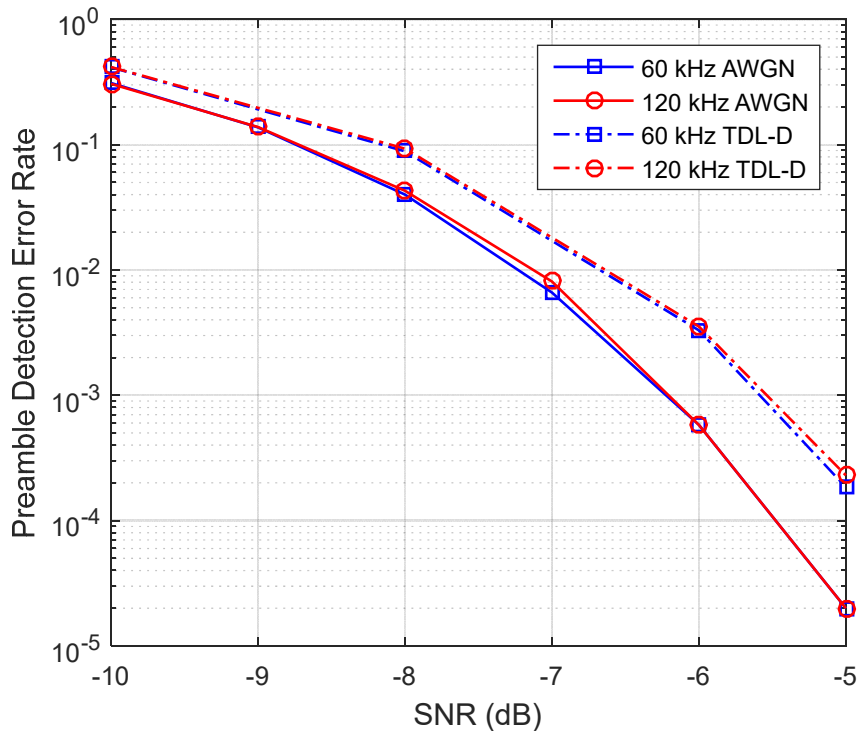


**Figure 37. Performance comparison with different preamble subcarrier spacing under AWGN and TDL-D channels**

Figure 37 shows the preamble detection error rate with different preamble subcarrier spacings under various channel environments. Generally, we can observe that the performance between different subcarrier spacings are quite close to each other in both AWGN and TDL-D channels. The reason is that these performance results are obtained by Monte-Carlo simulations and the results come from an average of tens of thousands of iterations with different roots for the sequence generation. Also the performance is not sensitive to the frequency offset due to the aforementioned fact that the theoretical maximum frequency offset considered in the simulations are less than 40% of subcarrier spacing 60 kHz and 20% of 120 kHz. So that the correlation peaks of different sequences generated by using different roots are good enough for distinguishing the transmitted sequences. When comparing the performances of these short preambles with conventional LTE performances with long sequences as shown in [54], we can observe obvious performance degradations, which may not only come from different simulation parameters adopted but also the shorter sequence length for generating preambles in our simulations. That is, shorter sequence length may lead to both worse correlation performance and less accumulated power. On the other hand, the observed performance employing short preamble sequence is still acceptable based on our understanding. Furthermore, this problem might be solved by employing another short preamble format, which contains more preamble symbols than the format A0, for implementation and performance optimization in a real system.



<b>Title:</b>	Deliverable D3.8: Final results on the mobility framework		
<b>Date:</b>	31 May 2018	<b>Status:</b>	Final
<b>Security:</b>	Public	<b>Version:</b>	V1.0

### 4.2.3 Handover triggering for mobility in 3GPP 5G NR HS scenario

#### 4.2.3.1 High speed scenario defined in 3GPP 5G NR

In [55], NR has defined a HS scenario originally for supporting robust wireless communications for HST passengers. Generally, there are two different network deployment scenarios for HST communications. Figure 38 shows the network deployment for a carrier frequency of 4 GHz, where each BBU connects with two RRHs. A BS, which is known as gNB in NR, contains BBU and one or several connected RRHs. In NR HS scenarios, RRHs are deployed along the rail track. The cell boundary in this deployment is in the center between two adjacent sites. Therefore, an overlapped cell boundary area between two adjacent sites exists, which is similar to the cell edge area in a cellular network. In the network deployment shown in this figure, the onboard UE can directly access the network, or the UEs can access the network through onboard MR stations. Figure 39 shows a network deployment in the 30 GHz frequency band. In this case, three RRHs are connected to a BBU and the network is deployed in a unidirectional manner. Therefore, the cell boundary is around the location of the adjacent RRH but not in the center area between two adjacent RRHs. Furthermore, onboard UEs can only access the network via a MR located on top of the carriages of a train.

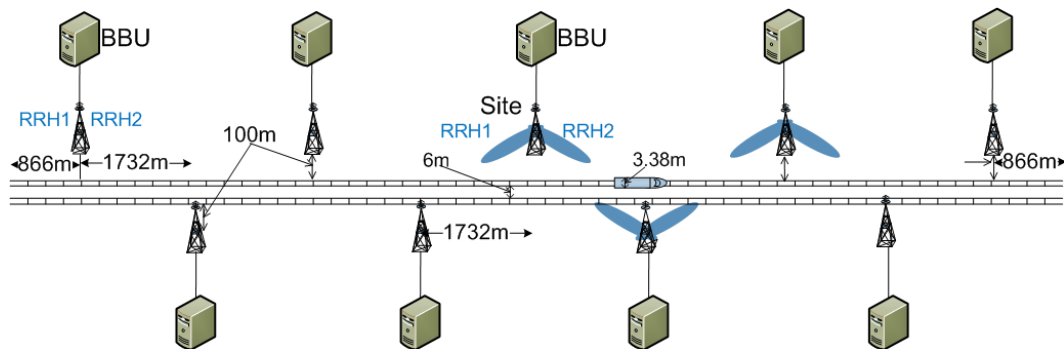


Figure 38. NR HS scenario bidirectional network deployment with 4 GHz carrier frequency

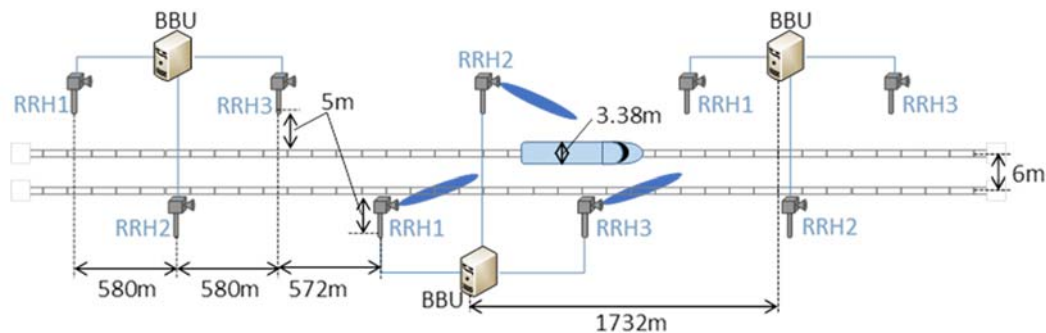


Figure 39. NR HS scenario unidirectional network deployment with 30 GHz carrier frequency

A big challenge exists if a traditional hard handover such as LTE handover is performed in a unidirectional network as shown in Figure 39, i.e., RLF during handover [56]. The reason is that the onboard UE/MR is always attempting to handover from a source cell with strong received power to a target cell with weak received power, in which case the UE/MR may not



<b>Title:</b>	Deliverable D3.8: Final results on the mobility framework		
<b>Date:</b>	31 May 2018	<b>Status:</b>	Final
<b>Security:</b>	Public	<b>Version:</b>	V1.0

be able to send back measurement reports (based on event A3 in LTE) to the source cell and receive a handover command from source cell. This problem can be observed in Figure 40, where the “desired gain” is from the source cell and “attempted gain” is from the target cell. In Figure 40, three RRHs are located at the location of -1000m, 0m, and 1000m, respectively, and a HST is moving from the left side to the right side within the area of [-1000m , 0m]. Therefore, novel handover triggering mechanisms for unidirectional network deployment are necessary considering that triggering the handover based on DL measurements of event A3 and report is not suitable any longer.

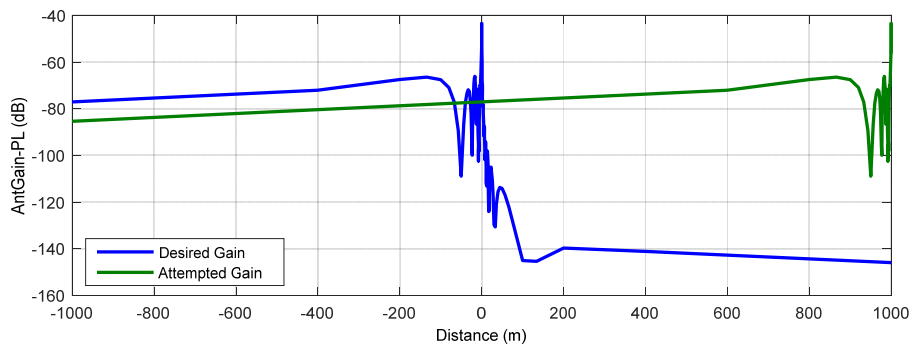


**Figure 40. An example of channel gain (combination of free-space path loss and directional antenna radiation pattern) observed by a moving HST**

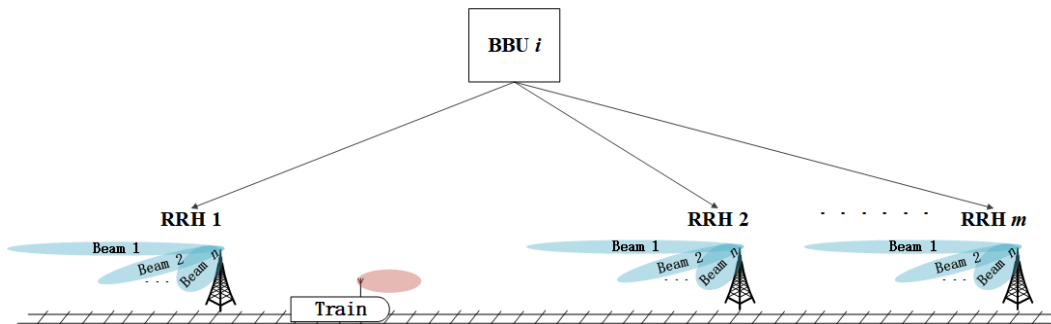


**Figure 41. Directional network deployment for HST communications with multi-beam operations**

#### 4.2.3.2 Proposed events for handover triggering in directional network

For simplifying the description, we show an example of unidirectional HST network structure for describing our proposals. As shown in Figure 41, the  $i$ -th BBU is connected to  $m$  RRHs along the rail track. A train is moving from the left side to the right side with an onboard MR, whose function is to deliver data between the terrestrial BS (a BS consists of a BBU and several connected RRHs) and the onboard UEs. Directional antennas are employed at both the MR and RRHs. In each RRH,  $n$  beams are generated through beamforming using directional antennas, such as panel antennas. Following the NR design, different SSBs can be transmitted through different beams at the RRH as a RS for beam measurement. Note

The information contained in this document is the property of the contractors. It cannot be reproduced or transmitted to thirds without the authorization of the contractors.



---

<b>Title:</b>	Deliverable D3.8: Final results on the mobility framework		
<b>Date:</b>	31 May 2018	<b>Status:</b>	Final
<b>Security:</b>	Public	<b>Version:</b>	V1.0

---

that other reference signals such as CSI-RS in NR can be used as a RS for measurement also.

#### **4.2.3.2.1 Handover triggering mechanism based on DL RSRP measurement**

In a unidirectional network, the UE/MR may measure an A3 event successfully. The problem of RLF is that the UE/MR measurement report may not be correctly sent to the gNB or the gNB command for triggering the handover may not be successfully delivered to the UE/MR. This failure of information/command exchange for handover triggering can be avoided if the handover triggering decision can be made by the UE/MR directly. That is, when a UE/MR measures an A3 event based on DL RSRP estimation, this UE/MR can make a decision for handover without reporting A3 to BS. Note that in the NR HST scenario, the RS used for DL measurement can be SSB, CSI-RS or other type of RSs.

#### **4.2.3.2.2 Handover triggering mechanism based on UL RSRP measurement**

An UL based RSRP measurement can be used for triggering the handover in unidirectional networks as well. In this case, the BS can measure the UL based on UL RS such as a SRS in NR. In this case, the handover triggering decision can be made by the BS when, for example, the UE/MR is moving near a cell boundary area. Since the RRHs are deployed along the rail track, the BS will be able to roughly know the location of the served UE/MR through distance estimation based on UL path loss (monitored UL RSRP for example). Therefore, this BS can send a handover triggering command to this specific UE/MR through DL signaling before it moves out of the serving cell coverage, and prepare for handover with the targeting BS via X2 interface.

#### **4.2.3.2.3 Handover triggering mechanism based on timing monitoring**

Except for the handover triggering based on RSRP measurements above, DL and UL timing might be used for triggering handovers also. The reason for employing timing monitoring is that the routes of HSTs are predictable and the RRHs are deployed along the rail track.

1. The BS can monitor the UL arrival timing of a UE/MR and trigger a handover based on UL timing. If the HST is moving towards RRHs, then the BS can trigger a handover if the TA value of UL approaches 0. The optimal TA value can be based on the real deployment. If the HST is moving toward the opposite direction of RRHs, then the BS can trigger a handover if the TA value of the UL approaches a specific value. This optimal TA value for triggering a handover can be considered as a new event for handover triggering. The benefit of this method is to avoid ping-pong effects during handover. After making a handover decision, the BS should inform the UE/MR with a handover command and request a handover to the targeting BS of this specific UE/MR.
2. Alternatively, the UE/MR can trigger a handover based on TA information from the BS. This specific TA for triggering a handover can be configured by the BS in prior, so that the UE/MR can know this specific TA value. In this case, no further information exchange is necessary for triggering a handover between the UE/MR and BS since both of them know the timing for the handover.

Note that the above example considers the employment of a TA in the system. It might be possible that a TA is not used in some specific systems. However, even if there is no TA in such a system, timing monitoring for DL and UL are still necessary for correctly decoding DL



---

<b>Title:</b>	Deliverable D3.8: Final results on the mobility framework		
<b>Date:</b>	31 May 2018	<b>Status:</b>	Final
<b>Security:</b>	Public	<b>Version:</b>	V1.0

---

and UL. Therefore DL or UL timing monitoring can still be used for triggering a handover in that system.

#### **4.2.3.2.4 Handover triggering mechanism based on beam index monitoring**

In a unidirectional network with multiple beams, as shown in Figure 41, the beam index information can be used for triggering a handover. When taking the HST scenario in NR systems as an example, assume that different SSBs are transmitted by different beams, and all the RRHs connected to the same BBU are considered as a single BS. Then,

1. The BS can trigger a handover when it monitors that the HST is served by its boundary beam. This DL beam information can be obtained through a UE/MR report, or a UL SRS measurement, or other kind of feedback from the UE/MR. If the HST is moving towards RRHs, then the boundary beam can be the n-th beam of the m-th RRH. If the HST is moving towards the opposite direction of RRHs, then the boundary beam can be the 1st beam of the 1st RRH. In this case, the serving BS can request a handover preparation from a neighboring BS. The serving BS may or may not need to inform the UE/MR of the handover triggering decision depending on whether the specific beam index information for triggering handover has been configured in the UE/MR in prior.
2. It also is possible that the UE/MR can trigger a handover by monitoring the serving DL beam index information. This beam index information can be obtained by detecting DL RSs/channels such as SSB, or from DL RSs, which is QCLed with SSBs such as CSI-RS, or from DL signaling. Similarly, the UE/MR may or may not need to send a handover request to the serving BS depending on whether this specific beam index information for handover triggering has been configured in the UE/MR in prior.

The specific beam for triggering a handover can be considered as a new handover triggering event, i.e., detection of a specific beam index for triggering a handover. In another word, the boundary beam for handover triggering can be considered as a special region, which is a handover zone.



<b>Title:</b>	Deliverable D3.8: Final results on the mobility framework		
<b>Date:</b>	31 May 2018	<b>Status:</b>	Final
<b>Security:</b>	Public	<b>Version:</b>	V1.0

---

## 5 Conclusion

In this deliverable, several important issues on channel modeling and mobility support for the high mobility scenario are investigated.

We first developed channel model targeted for the mmWave HST scenario. Extensive measurement campaigns are also conducted on an actual railroad. Extracted parameters includes path loss, RMS delay spread, RMS azimuth/zenith angle spread of arrival. These parameters are used for the channel model development using QuaDRiGa and the ray tracer calibration. The ray-tracing-based channel model is then used for the link-level performance evaluation of HST scenario. The results show that satisfactory link-level performance is attainable for the very high speed up to 500 km/h

We then investigated power-partitioning scheme that enables localization while transmitting its own data. Based on the tradeoff between localization efficiency and data rate, we proposed the improved transmit power partitioning scheme.

Further analysis on the HST scenario is done in terms of coverage and spectral efficiency. Using Nakagami-m fading model, coverage analysis results were provided. Also, using the 3GPP 5G NR channel model, spectral efficiency is provided based on MCS selection.

Lastly, random access procedure including preamble format design and handover triggering mechanism were studied. 3GPP 5G NR channel model was also employed for the performance evaluation.



---

<b>Title:</b>	Deliverable D3.8: Final results on the mobility framework		
<b>Date:</b>	31 May 2018	<b>Status:</b>	Final
<b>Security:</b>	Public	<b>Version:</b>	V1.0

---

## 6 References

- [1] M. Schmieder, M. Peter, R. Askar, I. Komsic, and W. Keusgen, "Measurement and characterization of 28 GHz High-Speed train backhaul channels in rural propagation scenarios," in 2018 12th European Conference on Antennas and Propagation (EuCAP 2018), London, United Kingdom (Great Britain), Apr. 2018.
- [2] H. Xiao, A. G. Burr, and L. Song, "A time-variant wideband spatial channel model based on the 3gpp model," in Vehicular Technology Conference, 2006. VTC-2006 Fall. 2006 IEEE 64th. IEEE, 2006, pp. 1–5.
- [3] N. Czink and C. Oestges, "The COST 273 MIMO Channel Model: Three kinds of clusters," in Spread Spectrum Techniques and Applications, 2008 IEEE 10th International Symposium on. IEEE, 2008, pp. 282– 286.
- [4] N. Czink, T. Zemen, J.-P. Nuutinen, J. Ylitalo, and E. Bonek, "A Time-Variant MIMO Channel Model Directly Parametrised from Measurements," EURASIP J. Wireless Commun. Netw., vol. 2009, no. 1, p. 687238, 2009.
- [5] K. Saito, K. Kitao, T. Imai, Y. Okano, and S. Miura, "The modeling method of time-correlated MIMO channels using the particle filter," in Vehicular Technology Conference (VTC Spring), 2011 IEEE 73rd. IEEE, 2011, pp. 1–5.
- [6] W. Wang, T. Jost, U.-C. Fiebig, and W. Koch, "Time-variant channel modeling with application to mobile radio based positioning," in Global Communications Conference (GLOBECOM), 2012 IEEE. IEEE, 2012, pp. 5038–5043.
- [7] S. Jaeckel, L. Raschkowski, K. Borner, and L. Thiele, "QuaDRiGa: A 3-D Multi-Cell Channel Model With Time Evolution for Enabling Virtual Field Trials," IEEE Trans. Antennas Propag., vol. 62, no. 6, pp. 3242–3256, 2014
- [8] Meinilä, J., Kyösti, P., Jämsä, T., & Hentilä, L. (2009). WINNER II channel models. Radio Technologies and Concepts for IMT-Advanced, 39-92.
- [9] 3GPP TR 36.873, v1.3.0, "Study on 3D channel model for LTE (Release 12)", February, 2014 (available at [www.3gpp.org](http://www.3gpp.org)).
- [10] 3rd Generation Partnership Project (3GPP), "3GPP TR 38.901 V14.2.0: Study on channel model for frequencies from 0.5 to 100 GHz," 3GPP, Tech. Rep., September 2017.
- [11] J. Yang, B. Ai, K. Guan, R. He, Z. Zhong, Z. Zhao, D. Miao, and H. Guan, "On the influence of mobility: Doppler spread and fading analysis in rapidly time-varying channels," *10th European Conference on Antennas and Propagation (EuCAP2016)*, Davos, Switzerland, pp. 1-5, April 2016.
- [12] P. Soma, L. C. Ong, S. Sun, and M. Y. W. Chia, "Propagation measurements and modeling of LMDS radio channel in singapore," *IEEE Trans. Veh. Technol.*, vol.52, no.3, pp.595–606, May 2003.
- [13] D. He, B. Ai, K. Guan, Z. Zhong, B. Hui, J. Kim, H. Chung, and I. G. Kim, "Channel measurement, simulation and analysis for high speed railway communications in 5G millimeter-wave band," *IEEE Trans. Intell. Transp. Syst.*, to be published.



---

<b>Title:</b>	Deliverable D3.8: Final results on the mobility framework		
<b>Date:</b>	31 May 2018	<b>Status:</b>	Final
<b>Security:</b>	Public	<b>Version:</b>	V1.0

---

- [14] R. B. Ertel, P. Cardieri, K. W. Sowerby, T. S. Rappaport, and J. H. Reed, "Overview of spatial channel models for antenna array communication systems," *IEEE Personal Commun.*, vol.5, no.1, pp.10–22, Feb. 1998.
- [15] 3GPP TR 38.913, "Study on Scenarios and Requirements for Next Generation Access Technologies," June 2016.
- [16] 3GPP TR 38.901, "Study on channel model for frequencies from 0.5 to 100 GHz", December 2017.
- [17] J. Kim and I. G. Kim, "Distributed antenna system-based millimeter-wave mobile broadband communication system for high speed trains," in *2013 International Conference on ICT Convergence (ICTC)*, Jeju, 2013, pp. 218-222.
- [18] Y. Li, et al., "On the initial access design in millimeter wave cellular networks," in *IEEE GLOBECOM Wkshps.*, 2016, pp. 1–6.
- [19] G. Ghatak, A. De Domenico and M. Coupechoux, "Coverage Analysis and Load Balancing in HetNets with mmWave Multi-RAT Small Cells," *IEEE Trans. Wireless Commun.*, 2018.
- [20] N. Garcia, et al., "Location-aided mm-wave channel estimation for vehicular communication," in the *IEEE 17th International Workshop on Signal Processing Advances in Wireless Communications (SPAWC)*, 2016, pp. 1–5.
- [21] G. Destino and H. Wymeersch, "On the trade-off between positioning and data rate for mm-wave communication," in *2017 IEEE International Conference on Communications Workshops (ICC Workshops)*, May 2017, pp. 797–802.
- [22] 5G CHAMPION, "D3.7 Preliminary results on the mobility framework" June 2017.
- [23] S. Jeong, et al., "Beamforming design for joint localization and data transmission in distributed antenna system," *IEEE Transactions on Vehicular Technology*, vol. 64, no. 1, pp. 62–76, 2015.
- [24] F. Lemic, et al., "Localization as a feature of mmwave communication," in *Wireless Communications and Mobile Computing Conference (IWCMC)*, 2016 International. IEEE, 2016, pp. 1033–1038.
- [25] R. Koirala, et al., "Localization bound based beamforming optimization for multicarrier mmwave mimo," in *2017 14th Workshop on Positioning, Navigation and Communications (WPNC)*, Oct 2017, pp. 1–6.
- [26] T. Bai and R. W. Heath, "Coverage and Rate Analysis for Millimeter-Wave Cellular Networks," *IEEE Trans. Wireless Commun.*, vol. 14, no. 2, pp. 1100–1114, 2015.
- [27] H. Elshaer, et al., "Downlink and Uplink Cell Association With Traditional Macrocells and Millimeter Wave Small Cells," *IEEE Trans. Wireless Commun.*, vol. 15, no. 9, pp. 6244–6258, Sept. 2016.
- [28] Y. J. Chun, M. O. Hasna, and A. Ghayeb, "Modeling heterogeneous cellular networks interference using poisson cluster processes," *IEEE J. Sel. Areas Commun.*, vol. 33, no. 10, pp. 2182–2195, 2015.
- [29] G. Ghatak, A. D. Domenico, and M. Coupechoux, "Modeling and analysis of hetnets with mm-wave multi-rat small cells deployed along roads," in *GLOBECOM 2017*, Dec 2017, pp. 1–7.



---

<b>Title:</b>	Deliverable D3.8: Final results on the mobility framework		
<b>Date:</b>	31 May 2018	<b>Status:</b>	Final
<b>Security:</b>	Public	<b>Version:</b>	V1.0

---

- [30] S. N. Chiu, et al., Stochastic geometry and its applications. John Wiley & Sons, 2013.
- [31] J. G. Andrews, et al., "Modeling and analyzing millimeter wave cellular systems," IEEE Transactions on Communications, vol. 65, no. 1, pp. 403–430, Jan 2017.
- [32] A. Dammann, et al., "Optimizing waveforms for positioning in 5g," in IEEE 17th International Workshop on Signal Processing Advances in Wireless Communications (SPAWC), July 2016, pp. 1–5.
- [33] K. Wu, et al., "Fila: Fine-grained indoor localization," in INFOCOM, 2012 Proceedings IEEE. IEEE, 2012, pp. 2210–2218.
- [34] T. S. Rappaport et al., "Millimeter wave mobile communications for 5G cellular: It will work!" IEEE Access, vol. 1, pp. 335–345, May 2013.
- [35] M. Akdeniz et al., "Millimeter wave channel modeling and cellular capacity evaluation," IEEE J. Sel. Areas Commun., vol. 32, no. 6, pp. 1164–1179, Jun. 2014.
- [36] T. Bai and R. W. Heath, "Coverage and rate analysis for millimeter-wave cellular networks," IEEE Trans. Wireless Commun., vol. 14, no. 2, pp. 1100–1114, Feb. 2015.
- [37] J. G. Andrews et al., "What will 5G be?" IEEE J. Sel. Areas Commun., vol. 32, no. 6, pp. 1065–1082, Jun. 2014.
- [38] T. Bai, A. Alkhateeb, and R. W. Heath, "Coverage and capacity of millimeter-wave cellular networks," IEEE Commun. Mag., vol. 52, no. 9, pp. 70–77, Sep. 2014.
- [39] Z. Xiao, L. Bai, and J. Choi, "Iterative joint beamforming training with constant-amplitude phased arrays in millimeter-wave communications," vol. 18, no. 5, pp. 829–832, May 2014.
- [40] L. Yang and M.-S. Alouini, "Performance analysis of multiuser selection diversity," IEEE Trans. Veh. Technol., vol. 55, no. 6, pp. 1848–1861, Nov. 2006.
- [41] P. Viswanath, D. N. C. Tse, and R. Laroia, "Opportunistic beamforming using dumb antennas," IEEE Trans. Inf. Theory, vol. 48, no. 6, pp. 1277–1294, Jun. 2002.
- [42] I. S. Gradshteyn and I. M. Ryzhik, Tables of Integrals, Series, and Products, 7th ed. London, UK: Academic Press, 2007.
- [43] 3GPP TR 38.900, "Study on channel model for frequency spectrum above 6 GHz," v. 14.3.1, Jul. 2017.
- [44] 3GPP TR 38.802, "Study on new radio NR access technology; physical layer aspects," v. 14.1.0, Jun. 2017.
- [45] 3GPP, "WF on CDL-D model for high speed train scenario at 30GHz for RRH and relay," R1-168174, Aug. 2016.
- [46] R1-163984, "Discussion on phase noise modeling," RAN1#85, May 2016.
- [47] RP-160671, "Next Generation New Radio Access Technology," NTT DOCOMO, March, 2016.
- [48] RP-170847, "New WID on New Radio Access Technology," NTT DOCOMO, March, 2017.
- [49] 3GPP TS 38.211, "NR; Physical channels and modulation," V1.2.0, Release 15, Nov. 2017.



---

<b>Title:</b>	Deliverable D3.8: Final results on the mobility framework		
<b>Date:</b>	31 May 2018	<b>Status:</b>	Final
<b>Security:</b>	Public	<b>Version:</b>	V1.0

---

- [50] 3GPP TS 38.212, "NR; Multiplexing and channel coding," V1.2.0, Release 15, Nov. 2017.
- [51] 3GPP TS 38.213, "NR; Physical layer procedures for control," V1.2.0, Release 15, Nov. 2017.
- [52] 3GPP RAN1 meeting #86bis, R1-1610986, "WF on updated link level evaluation assumptions for RACH preamble", Lisbon, Portugal, Oct. 2016.
- [53] 3GPP TR 38.900, "Study on channel model for frequency spectrum above 6 GHz (Release 14)".
- [54] T. Li, et. al., "An improved preamble detection method for LTE PRACH in high-speed railway scenario," in *Proc. International Conference on Communications and Networking in China* (ChinaCom 2015,) Aug., 2015.
- [55] 3GPP TR 38.913, "Study on scenarios and requirements for next generation access technologies (Release 14)".
- [56] 3GPP RAN4 Meeting #77, R4-158179, "HST ad hoc minutes," Anaheim, USA, 16-20 Nov, 2015.
- [57] G. Ghatak et al. "Positioning Data-Rate Trade-off in mm-Wave Small Cells and Service Differentiation for 5G Networks," IEEE VTC spring 2018.